

Cite this: *Catal. Sci. Technol.*, 2022,
12, 5723

Isotopic evidence for the tangled mechanism of the CO-PROX reaction over mixed and bare cobalt spinel catalysts†

Camillo Hudy,^{id} Joanna Gryboś,^{id} Kim Steenbakkens, Kinga Góra-Marek,^{id}
Filip Zasada^{id} and Zbigniew Sojka^{id*}

The catalytic performance of the bare Co_3O_4 and mixed cobalt-spinel catalysts ($\text{M}_x\text{Co}_{3-x}\text{O}_4$; $\text{M} = \text{Cr}, \text{Mn}, \text{Fe}, \text{Ni}, \text{Cu}, \text{Zn}$) in the CO-PROX process was investigated in the temperature-programmed surface reaction (TPSR) mode using $^{18}\text{O}_2$ as an oxidant. The developed heuristic approach, where the prototype isotopic compositions of the reaction products ($\text{C}^{16}\text{O}^{18}\text{O}$, C^{16}O_2 , C^{18}O_2 , H_2^{16}O and H_2^{18}O), inferred from a conceivable molecular course of the postulated catalytic scenarios, are confronted with the experimental data allows for delineation of the CO-PROX reaction mechanism. For this purpose, in addition to mixed spinels, several intentionally labeled isotopic $^{18}\text{O}_2/\text{Co}_3^{18}\text{O}_4$, $^{16}\text{O}_2/\text{Co}_3^{18}\text{O}_4$, $^{18}\text{O}_2/\text{Co}_3^{16}\text{O}_4$ reference CO-PROX systems were examined. It was shown that the catalytic turnovers of CO and H_2 result from various combinations of the generic intrafacial Mars van Krevelen and suprafacial Langmuir–Hinshelwood/Eley–Rideal patterns, where the formation of surface carbonates as a common key intermediate allows for successful reproduction of the observed variation of the isotopic composition of CO_2 and H_2O with the selectivity. The mechanistic proposals were substantiated by DFT+U and *ab initio* thermodynamic modeling, corroborated by IR studies, which provided the requisite theoretical background for the dual role of the carbonate species as intermediates or spectators in the CO-PROX reaction, depending on their mode of attachment on the catalyst surface.

Received 13th June 2022,
Accepted 31st July 2022

DOI: 10.1039/d2cy01063a

rsc.li/catalysis

1. Introduction

The removal of residual carbon monoxide from bulk hydrogen *via* catalytic preferential oxidation (CO-PROX) is widely recognized as one of the most attractive technologies for the purification of industrial H_2 streams,^{1–3} for applications in PEMFC cells as a fuel or as a reactant in NH_3 synthesis, for example.^{4,5} Successful development of new efficient CO-PROX catalysts is primarily conditioned by an in-depth understanding of the reaction mechanism that governs the catalyst performance. It belongs, therefore, to one of the prime challenges of the recent catalytic chemistry of industrial hydrogen refinement.^{4–7}

Transition metal oxides are widely used for the development of model and applied catalytic materials with promising total CO oxidation^{8–13} and CO-PROX activities.^{5,14,15} Among many oxide systems, supported $\text{CuO}_x/\text{CeO}_2$ catalysts are undoubtedly the most explored, due to the beneficial effect of combining the active CuO phase with the CeO_2 support, which is

characterized by oxygen release and storage capacity.^{16,17} Another attractive group of CO-PROX catalysts that have been recently widely investigated are perovskites (ABO_3)^{18–20} and spinels (AB_2O_4).^{21–23} Upon proper selection of the A and B redox cations, the catalytic performance of such materials may be modified in the intended fashion. Further tuning is achieved by synthesis of mixed perovskite ($\text{A}_{1-x}\text{M}_x\text{B}_{1-x}\text{M}'_x\text{O}_3$) or spinel systems ($\text{A}_{1-x}\text{M}_x\text{B}_{2-x}\text{M}'_x\text{O}_4$), which also allows for regulation of the valence and coordination environment of the parent A and B cations. In this way by controlling the formation of various surface reactive oxygen species (ROS) and oxygen vacancies (V_O),^{24–26} whose particular involvement plays a crucial role in CO and H_2 oxidation,²⁷ the course of the CO-PROX reaction can be changed for a purpose. A vast number of various bulk spinels, such as Co_3O_4 ,²⁸ $\text{Au}/\text{Co}_3\text{O}_4$,³ CuFe_2O_4 ,²⁹ NiFe_2O_4 ,³⁰ $\text{Zn}_x\text{Co}_{3-x}\text{O}_4$ and $\text{Zn}_x\text{Co}_{3-x}\text{O}_4$,³¹ $\text{Co}_3\text{O}_4\text{-CeO}_2$ (ref. 32) or $\text{Co}_3\text{O}_4\text{-CuO}$,³³ as well as supported spinel-based catalysts, like $\text{CuMn}_2\text{O}_4/\text{CeO}_2$,³⁴ $\text{Co}_3\text{O}_4/\text{ZrO}_2$ and $\text{Co}_3\text{O}_4/\text{CeO}_2\text{-ZrO}_2$ (ref. 35) or $\text{ZnCo}_3\text{O}_4/\text{Al}_2\text{O}_3$ (ref. 36) for instance, have been investigated on this simple conceptual basis, demonstrating promising CO-PROX performance.

The three main types of surface reactions that can take place during the CO-PROX process include, in addition to the desired selective oxidation of carbon monoxide ($\text{CO} + 1/2\text{O}_2$

Faculty of Chemistry, Jagiellonian University, Gronostajowa 2, 30-387 Krakow, Poland. E-mail: sojka@chemia.uj.edu.pl

† Electronic supplementary information (ESI) available. See DOI: <https://doi.org/10.1039/d2cy01063a>



→ CO₂), the undesired H₂ oxidation (H₂ + 1/2O₂ → H₂O) and CO hydrogenation (CO + 3H₂ → CH₄ + H₂O), which lead to loss of hydrogen.^{23,37} The relative rates of these reactions depend critically on the changes in the redox and valence state of the cations constituting the spinel catalysts during the progress of the CO-PROX process with increasing temperature. Furthermore, as they can occur in a parallel way, or more likely be mechanistically intermingled, the native high activity of, e.g., Co₃O₄ toward CO oxidation is significantly perturbed in the presence of H₂.³⁸ In analogy to catalytic oxidation reactions,³⁹ the CO-PROX mechanism is treated by involving an intrafacial (Mars–van Krevelen) and/or a suprafacial (Langmuir–Hinshelwood/Eley–Rideal) pathway of CO and H₂ oxidation whose participation is controlled by the catalyst structure and the reaction conditions.^{28,40–43} Most postulates favor the operation of a redox mechanism of the CO-PROX reaction over transition oxide catalysts, which is based on the Mars van Krevelen (MvK) scheme.^{7,13,14} It has also been frequently proposed for cobalt spinel systems.^{23,44,45} Because the MvK mechanism involves the direct participation of lattice oxygen (O_{surf}²⁻) in the CO-PROX reaction, the created oxygen vacancies must be replenished by the gas phase O₂ efficiently enough to sustain the turnover of the reaction. As a result, the catalyst reoxidation capacity, which is often gauged by the isotopic surface oxygen exchange rate, exerts a direct impact on the catalytic performance.⁷ However, noting the facile formation and sufficient thermal stability of various reactive oxygen species on the most abundant (100) and (111) surfaces of cobalt spinel in the CO-PROX temperature window,²⁹ the operation of the Langmuir–Hinshelwood (LH) mechanism and its Eley–Rideal (ER) variant should also be taken into account in comprehensive mechanistic investigations using spinel catalysts. Indeed, it has been recently discussed, based on extensive DFT modeling, that CO may be oxidized in a multistep fashion by involving various combinations of the intrafacial MvK and suprafacial LH or ER mechanisms,⁴⁶ which leads to blurring of the CO-PROX reaction categorization in terms of a single mechanism only.

Catalytic studies with isotopically labeled reactants are particularly valuable but still scarcely applied for resolving the mechanistic issues of the CO-PROX reaction.^{43,47–49} In this work, we investigate the mechanism of the CO-PROX reaction on mixed cobalt spinel catalysts using ¹⁸O₂ as an oxidant. Metal ions (Cr, Mn, Fe, Co, Ni, Cu and Zn) of various electronic configurations (3d⁵–3d¹⁰) were introduced into the cobalt spinel matrix and screened for preferential CO oxidation with isotopic resolution. The guiding concept of these studies was to perturb the CO-PROX reaction course by doping the parent Co₃O₄ with foreign cations, to obtain information on the mechanistic details, by analyzing the response of the isotopic CO₂ and H₂O profiles to the reaction temperature and catalyst selectivity. Several reference experiments using various combinations of the isotopically labelled reactants (¹⁶O₂/Co₃¹⁸O₄, ¹⁸O₂/Co₃¹⁸O₄, ¹⁸O₂/Co₃¹⁶O₄, CO₂ + ¹⁸O₂/Co₃¹⁶O₄, CO₂/Co₃¹⁸O₄) and the parent cobalt

spinel were also performed to support the proper understanding of the CO-PROX mechanism. The goal of this paper is also to reveal its possible alteration, induced by the ubiquitous variation of the redox properties of the reaction mixture with the progression of conversion, and to recognize surface intermediates that are common for both CO and H₂ turnovers. The paper is organized in the following way. In chapter 3.1 the characterization of catalysts is briefly recalled, and chapter 3.2 describes rough isotopic data. The next chapter (3.3) presents the results of auxiliary and reference isotopic scrambling experiments together with isotopic data interpretation and comprehensive mechanistic considerations concluded by simulations of the isotopic profiles. Chapter 3.4 presents the corroborative results of DFT and *ab initio* thermodynamics modelling, and the overall diagram summarizing the key features of the proposed CO-PROX mechanism.

2. Experimental

2.1. Materials

The mixed spinel catalysts of the general formula M_xCo_{3-x}O₄ (M = Cr, Mn, Fe, Ni, Cu, or Zn) were obtained *via* combustion synthesis as described in our previous paper in more detail.²⁷ Initially, to a mixture of M(NO₃)₂·nH₂O and Co(NO₃)₂·6H₂O (Sigma Aldrich) with a M/Co ratio of 0.5, dissolved in 15 ml of water, 3.34 g of citric acid (Sigma Aldrich) was added. The resultant gel was heated at 400 °C for 15 minutes, and the obtained spinel was ground and then calcined at 600 °C for 4 hours. The obtained M_xCo_{3-x}O₄ catalysts are referred to as Cr-Co, Mn-Co, Fe-Co, Ni-Co, Cu-Co and Zn-Co, depending on the type of the foreign cation. The selection of dopants was based on the electronic configuration ranging from 3d³ to 3d¹⁰ and these are the typical transition metal ions that produce mixed spinels with cobalt, often used as catalysts.

2.2. Methods

The catalytic tests were performed in a gradientless quartz reactor ($\phi = 16$ mm), using 200 mg of the sample in the form of a thin layer of ~2 mm height. The estimated Peclet (Pe ≈ 0.005) and Damkohler (Da ≈ 0.1) numbers confirm that a basically complete mixing regime was maintained during the catalytic measurements. The criterial numbers for the extra- and intragranular diffusion limitations were verified according to the Eurokin procedure⁵⁰ (with external mass transport efficiency = 0.99 and internal diffusion efficiency = 0.96) The following QMS (Hidden) signals at $m/z = 2$ (H₂), 4(He), 18(H₂¹⁶O), 32(¹⁶O₂), 40(Ar), 44(C¹⁶O₂), 20(H₂¹⁸O), 34(¹⁶O¹⁸O), 46(C¹⁶O¹⁸O), and 48(C¹⁸O₂) were recorded. For selectivity quantification, the background corrected CO and H₂ signals, I_{CO} and I_{H_2} , with the corresponding sensitivity factors f_{CO} and f_{H_2} , determined in separate calibration measurements, were applied. Since the isotopic compositions of CO₂ and H₂O were analysed separately, therefore inclusion of the sensitivity factors is actually not needed ($p_{i\%} = f_i I_i / \sum (f_j I_j) = I_i / \sum (I_j)$, $i = \text{CO}_2$ or H₂O, and j labels the



corresponding isotopomers). Since during the CO-PROX reaction the change in the H₂ concentration is quite small (<3%), its possible influence on the background modification can practically be neglected. The catalysts were conditioned by heating to 600 °C in 5% O₂ gas flow before the catalytic tests. The temperature range from 25 °C to 300 °C, with a heating rate of 10 °C min⁻¹, was applied. The total flow rate of 100 ml min⁻¹ was regulated by mass flow controllers (Bronkhorst), with the feed composition corresponding to CO oxidation (2% C¹⁶O and 2% ¹⁶O₂ in He), H₂ oxidation (5% H₂ and 5% ¹⁶O₂ in He), and CO-PROX (2% CO and 2% ¹⁶O₂ or ¹⁸O₂, 30% H₂ in He balance) reactions. The O₂ excess with respect to CO was equal to λ = 2, and the ¹⁸O₂ gas reactant was enriched in 97%. The δ₁₆(CO₂) value was determined as $[p_{\%}(\text{C}^{16}\text{O}^{18}\text{O}) + 2p_{\%}(\text{C}^{16}\text{O}_2)]/[p_{\%}(\text{C}^{16}\text{O}^{18}\text{O}) + 2p_{\%}(\text{C}^{16}\text{O}_2) + p_{\%}(\text{C}^{18}\text{O}_2)]$, where $p_{\%}$ indicates the corresponding molar fractions. The H₂O and TPD experiments were performed in the range from 100 °C to 500 °C, with a heating rate of 10 °C min⁻¹, with the samples saturated with 2% of H₂O at 100 °C prior to the TPD runs.

2.3. Molecular modeling

The parametrization of the DFT calculations and molecular models used in our theoretical calculations was adopted from our previous papers^{39,51,52} and they are recalled here briefly. We used the spin unrestricted GGA+U DFT method with the PW91 exchange-correlation functional,⁵³ implemented in the VASP package. We set the Hubbard *U* parameter to 3.0 eV for the Co ions, and we employed the Monkhorst–Pack⁵⁴ method with 5 × 5 × 5 and 5 × 5 × 1 grid sampling meshes for the bulk and the slab models, respectively. The cutoff energy, $E_{\text{cut}} = 500$ eV, and the Methfessel–Paxton smearing parameter $\sigma = 0.1$ eV were applied. The SCF criterion was set to 10⁻⁷ eV, and the geometry optimization convergence level to 10⁻⁵ eV. Surface slab models of the Co₃₀O₄₀ stoichiometry, terminated with the (100) plane, were constructed by cleaving the optimized bulk cobalt spinel with 15 Å of vacuum. In the slab model of a total of 11 atomic layers (thickness of about 10 Å) only the top three layers were optimized.

First principles thermodynamics. The interaction of the cobalt spinel (100) plane with gaseous molecules of the CO-PROX process under different conditions (T , p_x , $x = \text{CO}$, H₂, O₂, H₂O, CO₂) was accounted by first principles thermodynamics (FPT). Following this approach, the free enthalpy of adsorption of reactant x (ΔG) was expressed as a function of the (T , p_x) parameters and the number of involved molecules n :⁵⁵

$$\Delta G(p_x, T, n_x) = \Delta E_{\text{ads}} - n\Delta\mu_x(p_x, T)$$

In the above expression, ΔE_{ads} is a DFT calculated electronic energy of adsorption, whereas $n\Delta\mu_x(p_x, T)$ corresponds to a change in the chemical potential of the n molecules upon adsorption, and may be calculated applying statistical thermodynamics.⁵⁶ For each of the proposed

adsorption modes, the free enthalpy, $\Delta G(p_x, T, n_x)$, was plotted as a function of T and p_x .

3. Results and discussion

3.1. Characterization of the mixed spinel catalysts

Thorough characterization of the examined spinel catalyst by spectroscopic XRF, RS, IR, XPS, structural (XRD) and microscopic techniques (SEM, TEM/STEM and EDX), supplemented by BET surface area measurements, has been reported in our previous paper.²⁷ The main results are succinctly recalled in the ESI† for convenience (chapter S1, Fig. S1 and S2, Table S1). Overall, the mixed spinel nanocrystals exhibit cuboctahedral shapes of quite uniform size of 20–27 nm for the Fe, Mn, and Cr-doped samples, and 47–52 nm for Ni, Cu and Zn-doped samples, including bare Co₃O₄. The XRD and RS results indicate that the Cr–Co, Mn–Co, and Fe–Co catalysts show the single spinel phase only, whereas in the case of Ni–Co, Cu–Co and Zn–Co segregated minor NiO, CuO and ZnO phases, apart from the dominant spinel one, were also observed (see Table S1†). Following the classification of spinels published earlier by us,²⁷ depending on the value of the oxygen u parameter (see Table S1,† and the definition of the u parameter given in its footnote), the catalysts with $u < 0.2625$ belong to type-B spinels (Cr–Co, Mn–Co and Fe–Co), which are characterized by the elongated edge sharing octahedra. Bare Co₃O₄ and the mixed Ni–Co, Cu–Co, and Zn–Co spinels with $u \sim 0.2625$, and a slight deformation of the octahedra only, belong to type-A. Both types of spinels exhibited different general behaviors in the CO-PROX reactivity, but their particular features are markedly controlled by the chemical nature of the dopant. Their catalytic behavior can be accounted for in terms of the electronic structure–reactivity relationship previously established by us, using heuristic descriptors based on the position of the oxygen 2p and the metal 3d band centers ($\Delta E_{\text{M-O}} = (E_{\text{M3d}} - E_{\text{O2p}})$), and the difference in the average electronegativity between the metal and oxygen ($E_{\text{O2p}} + k\Delta|\langle\chi_{\text{M}}\rangle - \chi_{\text{O}}|$).²⁷

3.2. Catalytic properties of the mixed spinels

In order to evaluate oxygen adsorption and surface dynamics in the temperature window of the CO-PROX process, the isotopic ¹⁶O₂/¹⁸O₂ exchange probe reaction over the synthesized mixed spinel catalysts was first carried out. The results obtained are presented in Fig. S3,† and are briefly discussed in the ESI† section S3. The experiments reveal that the A-type spinels are more active in catalyzing the dissociation of ¹⁶O₂ and ¹⁸O₂, and subsequent recombination of the ¹⁶O and ¹⁸O adatoms into the corresponding isotopomers, than the B-type spinels. A small effect of the Zn cations, which occupy exclusively the tetrahedral positions, and a large effect of the Cr and Mn cations located preferentially in the octahedral sites, suggest strongly that the edge-connected octahedra constitute a primary molecular playground where the dioxygen dissociation and

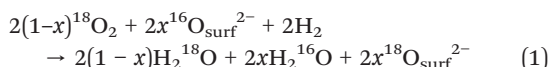


recombination processes, which are vital for the CO-PROX reaction, may occur.

The catalytic performance of the synthesized mixed spinels was examined in the CO-PROX reaction in our recent work, and thoroughly discussed.²⁷ For inspection, the conversion rates of CO and H₂ oxidation are shown in Fig. S4a and b,† together with the corresponding selectivities of the catalysts (Fig. S4c†). The presented conversion rate profiles clearly illustrate a pronounced influence of the dopant cations in the tetrahedral and octahedral sites on the catalytic activity in CO and H₂ oxidation for both A- and B-type spinels, among which the bare Co₃O₄ exhibits the best performance in terms of activity and selectivity at low temperatures.

In order to shed more light on the course of the investigated oxidation processes, we performed isotopic catalytic studies of the CO-PROX reaction, which were supported by reference CO and H₂ oxidation experiments using ¹⁸O₂ as an oxidant. Evolution of the C¹⁶O¹⁸O, C¹⁶O₂, C¹⁸O₂, H₂¹⁶O and H₂¹⁸O isotopomers with increasing temperature is shown in Fig. 1 for the parent Co₃O₄, and in Fig. 2 for the related mixed spinel samples.

Inspection of the results shown in Fig. 1a indicates that oxidation of H₂ by ¹⁸O₂ leads to prevalent formation of H₂¹⁸O in the entire range of the reaction, which is in line with the operation of the preponderant suprafacial Langmuir–Hinshelwood/Eley–Rideal (LH/ER) mechanism.⁵² Small amounts of H₂¹⁶O (<12%) arise from the contribution of ¹⁶O₂ present in the gas mixture (3 mol%), and an isotopic exchange, *x*, of the adsorbed reactive oxygen (¹⁸O_{2ads}) with the spinel surface ¹⁶O_{surf}²⁻ anions,



From the ratio of $p(\text{H}_2^{18}\text{O})/p(\text{H}_2^{16}\text{O}) = 4.70$, it can be inferred that $x \sim 0.14$ (upon correction for 97% of the ¹⁸O₂ enrichment) at 250 °C, that is, the terminal temperature of the CO-PROX reaction.

Isotopic composition profiles for CO oxidation with ¹⁸O₂ are, overall, dominated by the C¹⁶O¹⁸O isotopomer with the

C¹⁶O₂ fraction greater than that due to C¹⁸O₂ (Fig. 1b). The observed development of the abundant C¹⁸O₂ isotopomer cannot be explained by the operation of a simple MvK mechanism only. Possibly, it can arise from an isotopic exchange of CO₂ with the ¹⁸O_{ads} species, produced upon ¹⁸O₂ dissociation (C¹⁶O¹⁸O_{ads} + ¹⁸O_{ads} → C¹⁸O₂ + ¹⁶O_{ads}), or from the decomposition of a carbonate intermediate produced in the reaction between CO and ¹⁸O₂ adspecies, which is resolved below.

In the case of the CO-PROX reaction carried out with ¹⁸O₂ (Fig. 1c), the sequence of the carbon dioxide isotopomers, in general, resembles that observed for the oxidation of CO alone ($p(\text{C}^{16}\text{O}^{18}\text{O}) > p(\text{C}^{16}\text{O}_2) > p(\text{C}^{18}\text{O}_2)$) until ~180 °C. Above this threshold, the C¹⁶O₂ profile slightly declines, whereas the C¹⁸O₂ content develops steadily until full CO conversion is achieved. Finally, it leads to $p(\text{C}^{16}\text{O}^{18}\text{O}) > p(\text{C}^{18}\text{O}_2) > p(\text{C}^{16}\text{O}_2)$ in the high temperature range, in contrast to the single CO oxidation, where the relation $p(\text{C}^{16}\text{O}_2) > p(\text{C}^{18}\text{O}_2)$ is maintained through the whole reaction window. The formation of H₂O is markedly shifted toward higher temperatures, and the abundance of the evolving water isotopomers with $p(\text{H}_2^{16}\text{O}) > p(\text{H}_2^{18}\text{O})$ is reversed compared to the oxidation of sole H₂ (Fig. 1a). These results clearly reveal a strong reciprocal influence on the way in which H₂ and CO are oxidized when present simultaneously. Such observations are definitely confirmed by the fact that the isotopically resolved concentration profiles of carbon dioxide and water seen in the CO-PROX reaction (Fig. 1c) cannot be treated as a mere superposition of the corresponding profiles of the H₂O (Fig. 1a) and CO₂ (Fig. 1b) isotopomers when CO and H₂ are oxidized separately, even approximately. Supposedly, their co-oxidation is intricately in a common cycle by sharing a joint intermediate species, which cannot be accounted for by invoking a single MvK or LH/ER mechanism, operating in the whole CO-PROX reaction range.

For all the investigated mixed spinel catalysts (Fig. 2), the formation of the C¹⁶O¹⁸O isotopomer dominates, and the initial molar fraction of C¹⁶O₂ is higher than that of C¹⁸O₂, with the exception of the Cu–Co and Zn–Co samples. This

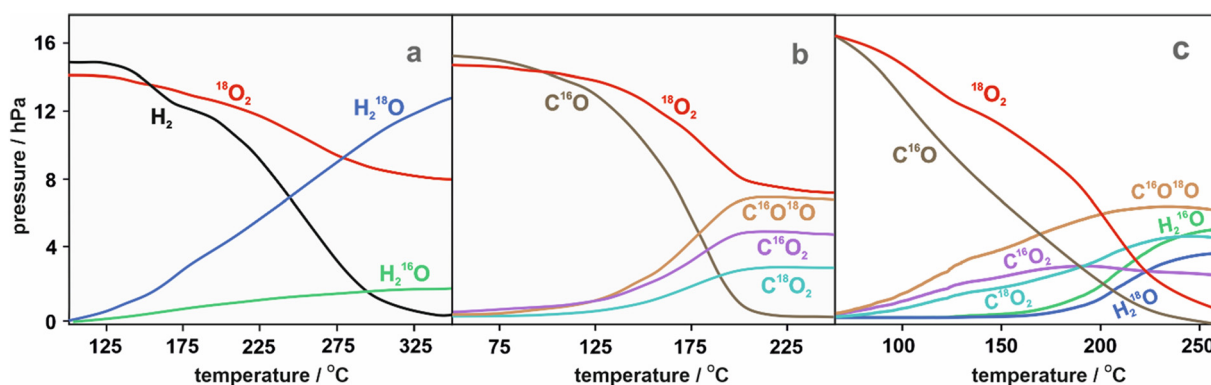


Fig. 1 Evolution of the reactant isotopic profiles with temperature for oxidation of sole H₂ (a), oxidation of sole CO (b), and during the CO-PROX reaction (c), over the parent Co₃O₄ catalyst using ¹⁸O₂ as an oxidant.



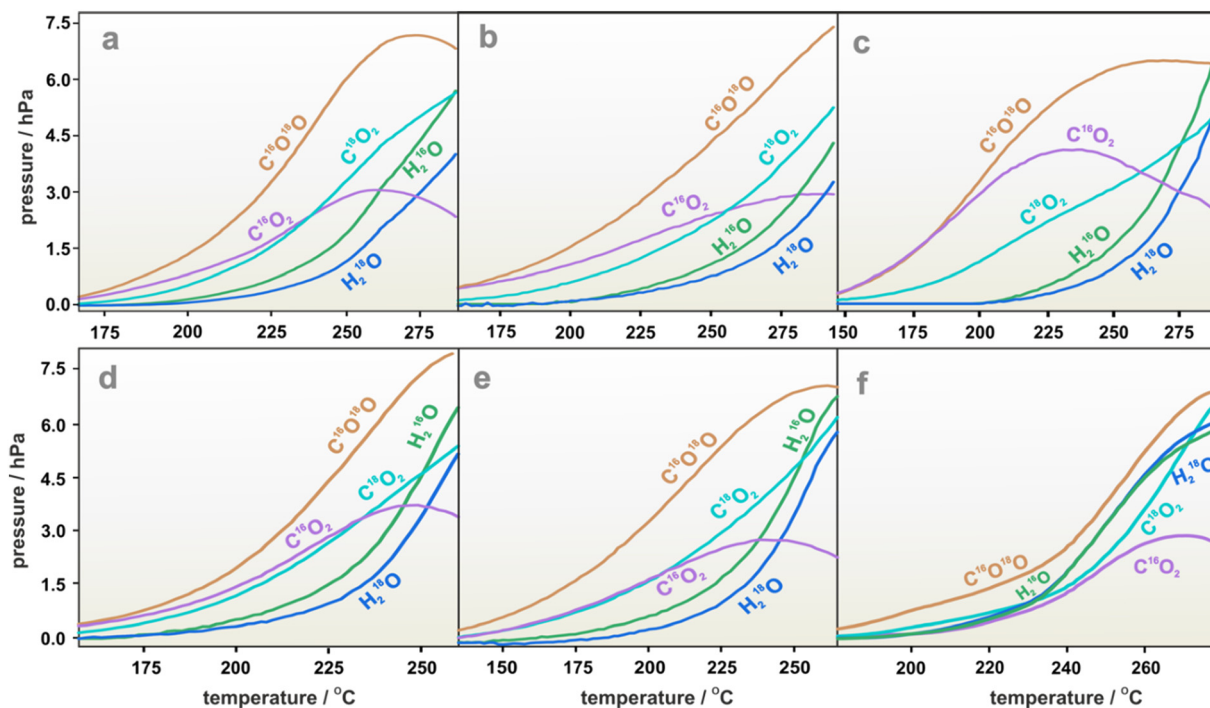


Fig. 2 Evolution of the $C^{16}O_2$, $C^{18}O_2$, $C^{16}O^{18}O$, $H_2^{16}O$ and $H_2^{18}O$ profiles with the temperature of the CO-PROX reaction using $^{18}O_2$ as an oxidant for Cr-Co (a), Mn-Co (b), Fe-Co (c), Ni-Co (d), Cu-Co (e), and Zn-Co (f) mixed spinels.

trend is reversed upon passing a threshold temperature (190–230 °C), from which $C^{18}O_2$ begins to prevail over $C^{16}O_2$. The actual value of the switching temperature depends on the nature of the co-cation, increasing in the order $Cr < Mn < Fe$ for the B-type spinels. In the case of the A-type spinels, the difference between the initial $C^{16}O_2$ and $C^{18}O_2$ contents declines for the Ni-Co catalyst, and is becoming practically insignificant for Cu-Co below 230 °C ($p(C^{16}O_2) \sim p(C^{18}O_2)$), see Fig. 2e. Above this temperature, $C^{18}O_2$ gradually exceeds the formation of $C^{16}O_2$. Remarkably, in the case of the unique Zn-Co catalyst, the formation of $C^{18}O_2$ dominates $C^{16}O_2$ in the whole temperature range of the PROX reaction ($p(C^{18}O_2) > p(C^{16}O_2)$). Analysis of the parallel water evolution profiles reveals that the $H_2^{16}O$ concentration is always higher than $H_2^{18}O$, again with the exception of the Zn-Co catalyst, where both water isotopomers are produced in nearly equal amounts. It should be emphasized that the isotopic composition of water with ($p(H_2^{16}O) > p(H_2^{18}O)$), is dramatically different from that observed for the oxidation of sole H_2 by $^{18}O_2$, which occurs primarily *via* the LH/ER mechanism (Fig. 1a).

Summarizing, the obtained isotopic results strongly suggest the operation of a complex mechanism of the CO-PROX reaction, which can only be resolved by assuming that the intrafacial or suprafacial pathways of the CO and H_2 turnovers operate concurrently. The particular relevance of each possible route varies with the temperature of the CO-PROX reaction, being apparently related to the reactant type (CO or H_2), and being distinctly modified by the catalyst nature (type of dopant) as well. Furthermore, the observed

strong and reciprocal influence of CO and H_2 on their oxidation process speaks in favor of mechanistic entanglement of these reactants into a common cycle that shares the same intermediates.

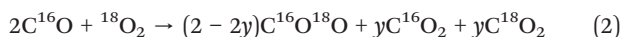
3.3. Mechanistic considerations

In the applied heuristic approach for the elucidation of the CO-PROX reaction mechanism, we analyzed conceivable catalytic scenarios of CO and H_2 oxidation, confronting the resulting prototype isotopic composition of the products with the experimental data as a function of the selectivity. Mechanistic considerations are based on critical evaluation of the following issues: (i) involvement of generic intrafacial (Mars van Krevelen) and suprafacial (Langmuir-Hinshelwood and/or Eley-Rideal) mechanisms, (ii) viability of an isotopic enrichment of the catalyst surface and isotopic scrambling of the reaction products, (iii) existence of a common intermediate that ensures mechanistic coupling of the concurrent CO and H_2 oxidation cycles, (iv) competition between CO and H_2 for scavenging of the surface O_{2ads}/O_{ads} species, and (v) possible parallel H_2 oxidation. Their particular relevance will be assessed based on the isotopically resolved composition of CO_2 and H_2O (expressed as the corresponding mole fractions) in the appropriate CO-PROX and the reference oxidation reactions of sole CO and H_2 with $^{18}O_2$. In the following text, the extent of surface isotopic enrichment in O-18 is labeled as x , and the extent of isotopic scrambling as y , whereas the fraction of the H_2 molecules oxidized together with CO is labeled by z . The later gauges

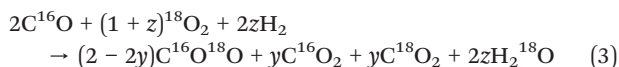


the conceptual selectivity used in the modeling as an independent variable. Additionally, a clear-cut distinction between the suprafacial Langmuir–Hinshelwood and Eley–Rideal mechanisms is not always possible, based on the present isotopic results only. Thus, they are labeled as a LH/ER pathway when appropriate, as one can easily evolve into another with increasing temperature.

Within the constraints imposed by the reaction stoichiometry, a single catalytic turnover of O₂ during the CO oxidation involves the transformation of two CO molecules to be fully accomplished (2CO + O₂ → 2CO₂). Thus, this process may be divided into 2 half-cycles, where two CO molecules are oxidized along the same or different pathways. Although, in the case of hydrogen oxidation, only two isotopomers (H₂¹⁶O and H₂¹⁸O) can be formed, this isotopic information plays a valuable ancillary restriction for the clarification of the CO-PROX reaction course. The appearance of H₂¹⁶O when ¹⁸O₂ is used as an oxidant is indicative of the participation of surface O_{surf}²⁻ during the oxidation of H₂ alone. In the CO-PROX reaction, however, H₂¹⁶O can be produced at the expense of O-16 originating from the C¹⁶O reactant, which provides an important hint for the mechanistic considerations. The more involved isotopic oxidation of CO, at the scrambling extent of $y \leq 0.5$, leads to conceivable formation of the following carbon dioxide species,



and $\delta_{16} = 0.5$, when the reaction is limited to the suprafacial (LH/ER) mechanism only. Deviations from this generic isotopic composition reflect the nature of the mechanism that actually operates. The values of $\delta_{16} > 0.5$ imply the participation of the surface oxygen in the reaction, which is often taken as an indication for the contribution of the Mars van Krevelen mechanism. Yet, the isotopic composition of CO₂ is substantially perturbed by the presence of H₂ in the reaction mixture, which is manifested by $\delta_{16} < 0.5$, when a CO and $z\text{H}_2$ molecules are oxidized by ¹⁸O₂ simultaneously,



then $\delta_{16} = 2/(4 + 2z) < 0.5$.

To assess the extent of the isotopic exchange of the CO₂ isotopomers with the surface O_{surf}²⁻ anions enriched in O-18 at the level of x , and scrambling with the oxygen adspecies, y , we performed auxiliary benchmarking TPSR studies taking the parent cobalt spinel as a convenient reference catalyst. These experiments include: (i) the scrambling reaction of C¹⁶O₂ with ¹⁸O₂ on Co₃O₄, (ii) the interaction of CO₂ and H₂O with the Co₃O₄ surface enriched in O-18, (iii) the ¹⁸O₂/CO-PROX reaction repeated on the Co₃O₄ catalyst, which was previously enriched in O-18 in the first run (see Fig. S5[†]), (iv) the ¹⁸O₂/CO-PROX, (v) ¹⁶O₂/CO-PROX reactions on fully isotopically labeled cobalt spinel (Co₃¹⁸O₄), and (vi) the isotopic scrambling of CO₂ and ¹⁸O₂ with the surface C¹⁸O₃²⁻

and C¹⁶O₃²⁻ carbonates, respectively. We also checked the possible influence of CO₂ and H₂O readsorption on the isotopic composition of the reaction products, by performing the relevant TPD experiments.

The Co₃¹⁸O₄ spinel was obtained by reduction of Co₃O₄ to metallic cobalt, and its subsequent complete reoxidation in the flow of ¹⁸O₂ to obtain an isotopically pure Co₃¹⁸O₄ catalyst. The corresponding TPSR profiles are shown in Fig. 3a–d.

The inspection of Fig. 3a shows that the suprafacial scrambling between CO₂ and ¹⁸O₂ is practically negligible throughout the temperature window of the CO-PROX reaction (marked in green), and therefore may reasonably be abandoned (y is close to 0). In turn, the intrafacial exchange of C¹⁶O₂ with the surface enriched in O-18 (during the prior CO-PROX reaction with ¹⁸O₂) becomes appreciable only above ~150 °C, changing non-monotonically with increasing temperature, with the maxima around 200 °C (broad), at 336 °C and at 401 °C (Fig. 3b), possibly associated with the presence of surface O_{surf}²⁻ anions in various topological locations. The extent of such exchange is, however, rather small in the CO-PROX reaction window (<3%). Accordingly, in this temperature range we also observed a slight enhancement of the C¹⁸O₂ content at the expense of the C¹⁶O¹⁸O and C¹⁶O₂ isotopomers in the second run of the CO-PROX reaction with ¹⁸O₂ (see Fig. S5[†]). We evaluated also the feasibility of a conceivable scrambling of C¹⁶O₂ with the O-18 labeled surface carbonates produced on Co₃¹⁸O₄ upon oxidation of CO with ¹⁸O₂, and scrambling of ¹⁸O₂ with the unlabeled surface carbonates (C¹⁶O₃²⁻). The results shown in Fig. S6a and b[†] indicate that such processes are negligible in the CO-PROX temperature window (marked in green), and that CO₂ is not appreciably re-adsorbed on the spinel surface. Only insignificant single exchange of ¹⁸O₂ with the spinel surface can be noticed (Fig. S6a[†]). In turn, scrambling of 2% H₂O with the Co₃¹⁸O₄ surface under flow conditions, and H₂¹⁶O desorption from Co₃¹⁸O₄ (Fig. S7a and b[†] respectively) confirm that the isotopic exchange of water with the spinel surfaces is also negligible. The desorption peak of water, after saturation of the surface with 2% of H₂O in the feed (the maximum concentration corresponding to the zero CO selectivity in PROX) appears around 140 °C. However, in this temperature region the H₂ conversion in CO-PROX is still very small (Fig. S4[†]). Thus, the contribution of minute quantities of the released water, which have been produced at low temperatures, to water formed at higher temperatures in more abundant amounts will not actually be relevant. These arguments are further reinforced by the thermodynamic modeling of surface coverage under varying water pressure, calculated from the experimental H₂ conversion during the CO-PROX reaction, which are discussed in the computational section below. Therefore, we presume that the adsorption/desorption processes are rather irrelevant for our isotopic analysis of the evolving water, which are limited to the results taken above 170–180 °C.

Hence, the performed numerous reference experiments show definitely that the isotopic compositions of CO₂ and H₂O are not significantly perturbed by the subsequent



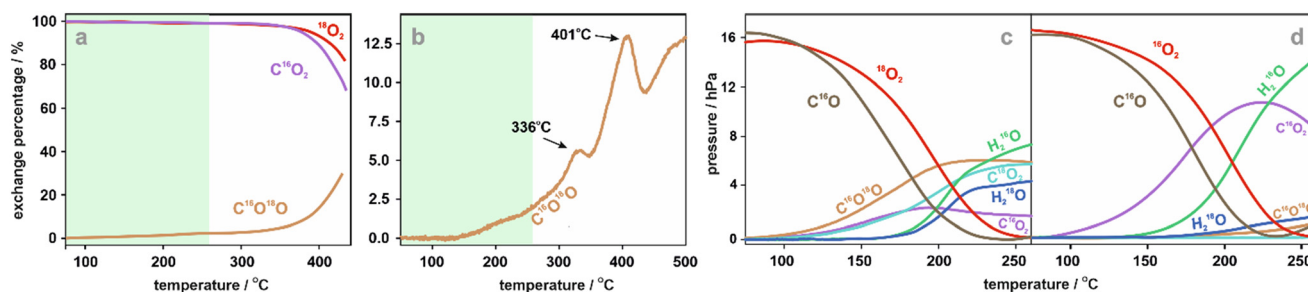


Fig. 3 TPSR profiles of the isotopic scrambling of $C^{16}O_2$ with $^{18}O_2$ (a), and with Co_3O_4 surface enriched in O-18 during the prior CO-PROX reaction with $^{18}O_2$ (b). TPSR profiles of the CO-PROX reaction performed with $^{18}O_2$ (c) and $^{16}O_2$ (d) on the $Co_3^{18}O_4$ catalyst.

scrambling with $^{18}O_2$ or by the interfacial isotopic exchange with the catalyst surface and/or carbonate intermediates, which are noticeable only at higher temperatures.

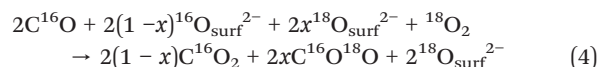
The spinel surface becomes appreciably enriched in O-18 during the CO-PROX reaction along two plausible channels. The most important one consists in refilling of the oxygen vacancies by $^{18}O_2$, which are produced when the MvK mechanism operates. An alternative scenario involves an isotopic exchange of the $^{18}O_{ads}$ intermediates (which appear during the CO-PROX reaction) with the surface $^{16}O_{surf}^{2-}$ anions. It has been demonstrated by us that such a process occurs with a rather small barrier ($E_a = 0.39$ eV) *via* transient $[^{18}O-O_{surf}]^{2-}$ peroxy species.⁵² The results of H_2 oxidation by $^{18}O_2$ shown in Fig. 1a indicate that the extent of the isotopic exchange should be below a few percent. As a result, in our further mechanistic considerations we presume that when the intrafacial MvK mechanism operates, the isotopic enrichment of the surface results mainly from the oxygen vacancy refilling, whereas in the case of the suprafacial LH/ER mechanism the isotopic exchange of $^{18}O_{ads}$ with $^{16}O_{surf}^{2-}$, which is responsible for the surface enrichment in O-18, can be abandoned, when it turns out to be necessary for the sake of the tractability of the results. Thus, the secondary scrambling of CO_2 with $^{18}O_2$ or with the surface enriched in O-18, disguising the mechanistic information, can be safely neglected. As a result, the isotopic compositions of carbon dioxide and water fairly well reflect the mechanistic pathways along which these CO-PROX reaction products are formed.

To check the possibility of a mechanistically critical transfer of O-16 coming from $C^{16}O$ into a water molecule, we examined the CO-PROX reaction with $^{18}O_2$ on the fully enriched $Co_3^{18}O_4$ catalyst (Fig. 3c). In such a case, CO is the only possible source of O-16, therefore, the results provide crucial information regarding the gross mechanistic features of the concomitant CO and H_2 oxidation. The appearance of $H_2^{16}O$, surprisingly at even higher amounts than $H_2^{18}O$, gives solid evidence that water is produced *via* H_2 interaction with the CO-derived intermediates, which are tentatively identified with the surface carbonates. The involvement of the carbonates may also explain the simultaneous formation of the $C^{16}O_2$ isotopomer in a straightforward way, since the development of these products ($C^{16}O_2$ and $H_2^{16}O$) could not be rationalized if CO was exclusively oxidized by $^{18}O_2$ directly

into CO_2 . The evolution of the isotopic profiles of $C^{16}O_2$ and $H_2^{16}O$ during the reaction of CO and H_2 with $^{16}O_2$ over the $Co_3^{18}O_4$ nanocrystals of the truncated cubic shape (Fig. 3d) illustrates a dominant participation of the suprafacial oxygen species when the (100) surface is preponderant (see microscopy results, Fig. S2e₄ and e₅†), which is especially apparent at lower temperatures of the CO-PROX reaction.

For further interpretation of the experimental results, we converted the isotopic profiles shown in Fig. 1–3c and d into the corresponding molar compositions (Fig. 4 and 5). In the latter figures, the evolution of the $\delta_{16}(CO_2)$ values with the progress of the reaction is also shown. Due to the complications resulting from an intricate course of the CO-PROX reaction, and the autogenous isotopic enrichment of the catalyst surface, sensible analysis based on a rigorous kinetic modeling of the isotopic CO_2 and H_2O profiles becomes extremely difficult to accomplish in a quantitative way. Instead, we analyzed the molar isotopic composition of the reaction products for conceivable mechanistic scenarios, assuming (i) direct oxidation of CO into CO_2 , (ii) CO dissociation and subsequent reoxidation, and (iii) indirect CO oxidation into CO_2 *via* carbonate intermediates, which have been reported in the literature.^{7,23,46,57} The route *via* the HCOO intermediates proposed in modeling the effect of water on CO oxidation on the (110) surface of Co_3O_4 (ref. 58) was neglected, noting the low abundance of such planes in our catalysts (see Fig. S2†), and the experimental isotopic composition of the reaction products. The relative isotopic compositions are not biased by the differences in the activation energies of CO (and H_2) oxidation over the particular mixed spinel, when it occurs along the same reaction pathway. However, the isotopic answer may possibly be disguised by parallel oxidation processes of different response to the increasing temperature, that accompany the main pathway. Inclusion of such effects requires more involved investigations, and they were not taken into account herein.

For direct CO oxidation into CO_2 , a Mars van Krevelen mechanism has often been proposed.^{7,9,23,41} As a result, when the catalyst surface becomes isotopically enriched at a fraction x , this reaction can be formulated in a succinct form as



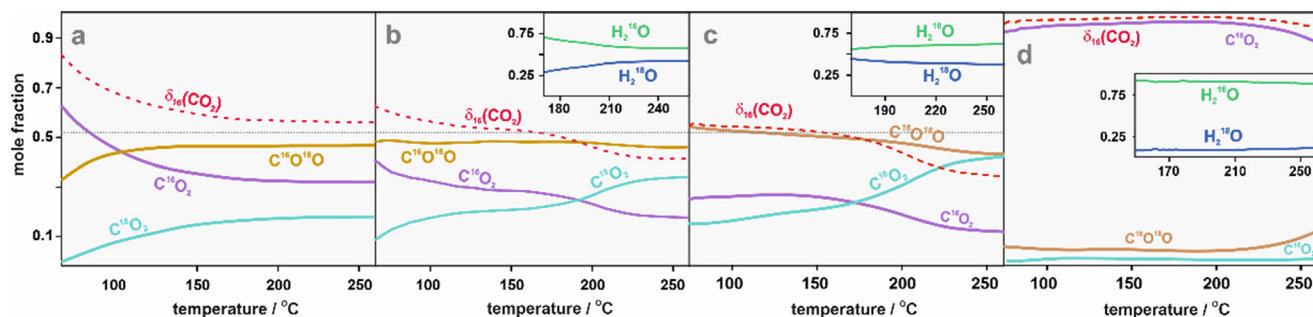


Fig. 4 Isotopic molar composition of the reaction products for the CO oxidation (a) and CO-PROX (b) reactions on Co_3O_4 using $^{18}\text{O}_2$ as an oxidant, and for the CO-PROX reaction performed with $^{18}\text{O}_2$ (c) and $^{16}\text{O}_2$ (d) on the $\text{Co}_3^{18}\text{O}_4$ catalyst. The dotted red lines indicate the temperature evolution of the $\delta_{16}(\text{CO}_2)$ profiles. Insets represent the isotopic composition of water.

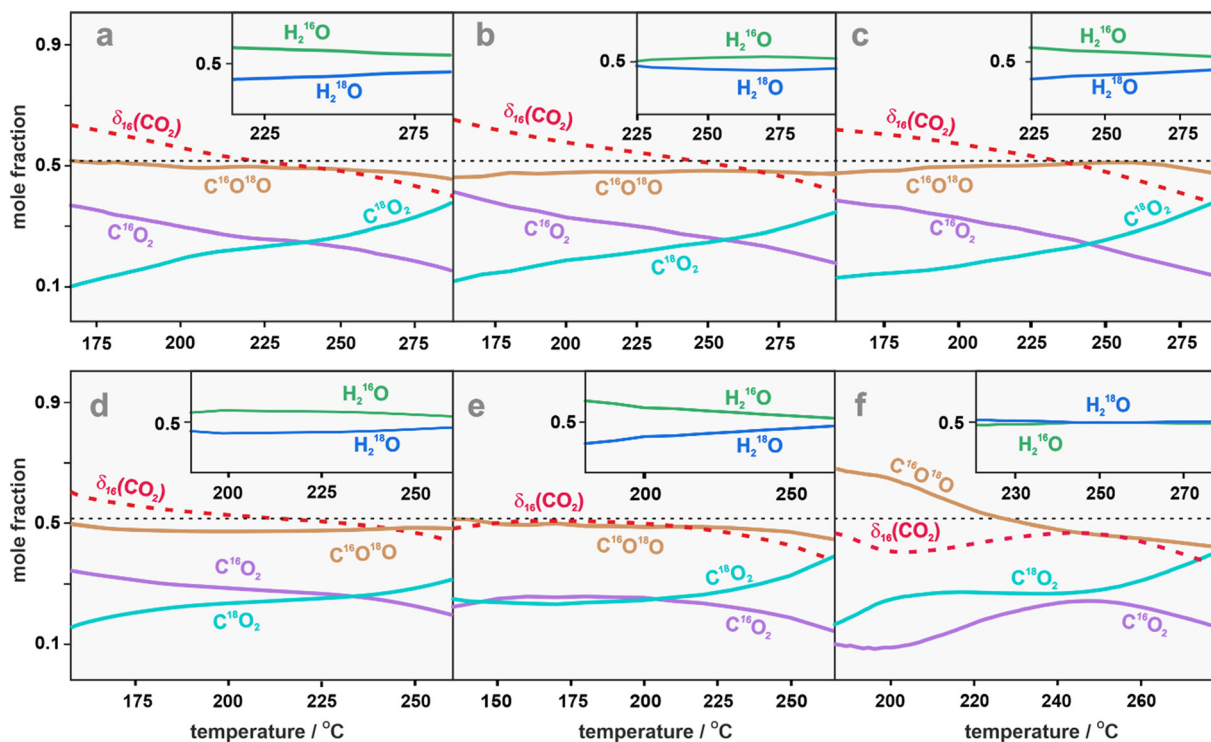
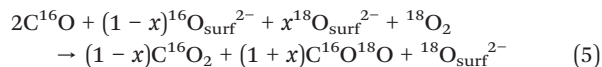


Fig. 5 Isotopic mole composition of the CO-PROX reaction products (CO_2 – main box and H_2O – insert) using $^{18}\text{O}_2$ as an oxidant for Cr-Co (a), Mn-Co (b), Fe-Co (c), Ni-Co (d), Cu-Co (e) and Zn-Co (f) catalysts. The dotted red line indicates the evolution of the $\delta_{16}(\text{CO}_2)$ profile.

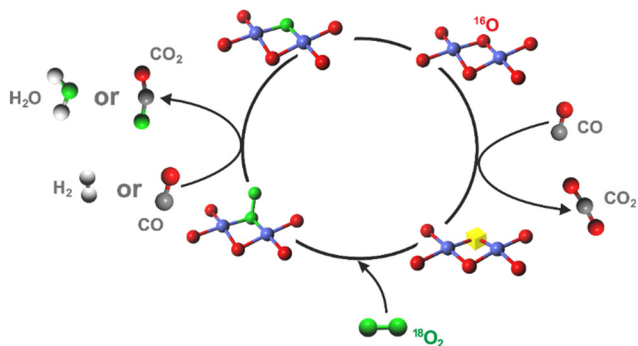
In this scheme, the oxygen vacancies, V_{O} , produced after CO oxidation by the $\text{O}_{\text{surf}}^{2-}$ species are refilled by gas phase $^{18}\text{O}_2$ in a 2:1 ratio, imposed by the stoichiometry: $^{18}\text{O}_2 + 2V_{\text{O}} \rightarrow 2^{18}\text{O}_{\text{surf}}^{2-}$. However, when the concentration of the oxygen vacancies is low, as reported elsewhere,⁵⁷ accommodation of an $^{18}\text{O}_2$ molecule while interacting with a vacancy assumes the 1:1 ratio ($^{18}\text{O}_2 + V_{\text{O}} \rightarrow ^{18}\text{O}_{\text{surf}}^{2-} + ^{18}\text{O}_{\text{ads}}$). The generated reactive $^{18}\text{O}_{\text{ads}}$ adspecies may next interact with the subsequent CO molecule, and the overall mechanism proceeds in the following way,



This pathway is actually tantamount to a coupled MvK and LH/ER mechanism (MvK-LH/ER), which is initiated by a MvK step and accomplished in a LH/ER one (see Scheme 1), as we cannot discriminate between the suprafacial LH and ER variants at this stage. An analogous mixed mechanism has previously been proposed for CO oxidation.⁵⁷ For the sake of conciseness the MvK-LH/ER mechanism will also be referred to briefly as an intrafacial mechanism, since the MvK step plays a key triggering role in its operation.

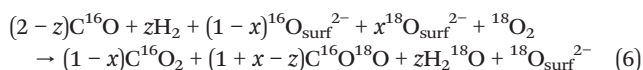
Denoting the molar composition of CO_2 as $p_{\%}$, the diagnostic characteristics of the intrafacial MvK-LH/ER mechanism are $p_{\%}(\text{C}^{16}\text{O}^{18}\text{O}) > p_{\%}(\text{C}^{16}\text{O}_2)$ and $p_{\%}(\text{C}^{18}\text{O}_2) \approx 0$, in contrast to the strict MvK pathway with $p_{\%}(\text{C}^{16}\text{O}_2) >$





Scheme 1 Direct oxidation of CO into CO₂ with ¹⁸O₂ via the intrafacial MvK-LH/ER mechanism in the presence of H₂. The catalyst surface becomes enriched in ¹⁸O eventually. Color coding: ¹⁶O - red, ¹⁸O - green, Co - blue, C - dark gray, H - pale gray balls.

$p_{\%}(C^{16}O^{18}O)$, when $x < 0.5$. The catalyst surface becomes enriched with O-18 in both cases, as seen in Fig. 4a, leading to $\delta_{16}(CO_2) > 0.515$ (considering 97% of the ¹⁸O₂ enrichment), and the formation C¹⁸O₂ is not predicted by these schemes. In the case of the CO-PROX reaction, the ¹⁸-O_{ads} intermediates may also be scavenged by zH₂ molecules (in competition with CO), which leads to the formation of H₂¹⁸O along with C¹⁶O₂ and C¹⁶O¹⁸O,



Consequently, the fraction of C¹⁶O₂ increases with the loss of the selectivity (increase in the H₂ conversion, see Fig. S4c†), whereas that of C¹⁶O¹⁸O decreases, giving rise to $p_{\%}(C^{16}O_2) > p_{\%}(C^{16}O^{18}O)$ and $p_{\%}(H_2^{18}O) \gg p_{\%}(H_2^{16}O) \approx 0$. Again, C¹⁸O₂ is not expected to be produced, and at the beginning of the CO-PROX reaction, when the H₂ conversion is negligible, $p_{\%}(C^{16}O_2) \sim p_{\%}(C^{16}O^{18}O)$. The loss of selectivity with increasing temperature, regardless of the particular reaction pathway (competitive H₂ oxidation or increasing isotopic enrichment of the surface due to the prior MvK step), leads to an increase in the C¹⁶O₂ contribution at the expense of C¹⁶O¹⁸O (in contrast to the experiment). As stated above, lower amounts of H₂¹⁶O may result from isotopic exchange of ¹⁸O_{ads} with ¹⁶O_{surf}²⁻ (see Fig. 1a), which is not included in eqn (6), for the sake of tractability.

The $\delta_{16}(CO_2)$ profile for the parent Co₃O₄ (Fig. 4b) implies, however, considerably greater involvement of the O_{surf}²⁻ in the reaction than in the case of Co₃¹⁸O₄ (Fig. 4c). This observation indicates that the MvK mechanism is more favored on the (111) surface than on the (100) termination, the abundance of which is decreased in the Co₃¹⁸O₄ sample. The Co₃¹⁸O₄ nano-crystallites exhibit a truncated cube shape, whereas the parent cobalt spinel a cuboctahedral one, as revealed by the TEM images (Fig. S2d and e†). This remains also in line with the lower onset of the reduction temperature of cobalt spinel nano-octahedra in comparison to nano-cubes, in parallel H₂-TPR experiments (results not shown).

None of the generic isotopic composition patterns predicted on the basis of the intrafacial MvK mechanism or its MvK-LH/ER option could fully be reconciled with the experimental results for the bare Co₃O₄ (Fig. 4b) and the mixed spinel catalysts (Fig. 5), as well. What is more important, CO cannot be directly oxidized into CO₂ as the main reaction channel, evidently. As it can be inferred from the comparison of Fig. 4a with 4b, the relative isotopic compositions of CO₂, and the $\delta_{16}(CO_2)$ profiles are strongly influenced by the H₂ co-reactant, and in this way by the catalyst selectivity. Remarkably, H₂ enhances the C¹⁸O₂ contribution but not that of C¹⁶O₂, whose formation is expected when the intrafacial (MvK and/or MvK-LH/ER) mechanism based on the direct oxidation of CO into CO₂ (eqn (4) and (5)) was engaged. Likewise, the isotopic composition of water with $p_{\%}(H_2^{16}O) > p_{\%}(H_2^{18}O)$, see the inserts in Fig. 4b and 5, cannot be resolved with any of the discussed options of the Mars van Krevelen mechanisms.

Another possible channel for CO oxidation via the MvK-LH/ER mechanism to be considered is represented by dissociation of a CO molecule adsorbed on the octahedral Co³⁺ center with an adjacent oxygen vacancy. The latter is produced during the earlier CO oxidation via O_{surf}²⁻ extraction. Such a mechanism has been proposed in the literature for CO oxidation over a Co₃O₄ catalyst, based on the carbon C1s signal detected during *in situ* NAP-XPS investigations.⁵⁷ The resultant putative Co-C moiety has been suggested to be oxidized directly into CO₂ by an O_{ads} and an O_{surf}²⁻ species. In such circumstances when ¹⁸O₂ is used, apart from C¹⁶O₂, a C¹⁶O¹⁸O isotopomer would also be formed simultaneously in an equal amount. Instead, if the bare carbon atoms were oxidized by direct association with ¹⁸O₂, the C¹⁶O¹⁸O species should not appear. The observed isotopic composition of carbon dioxide, with the persistent simultaneous presence of C¹⁸O₂ and C¹⁶O¹⁸O in the products regardless of the type of the catalyst and the reaction temperature (Fig. 2), indicates that such a channel is probably of marginal relevance for the CO-PROX reaction with $\lambda = 2$. Thus, it may reasonably be neglected, which is additionally substantiated by an unfavorable thermodynamics of CO insertion into the oxygen vacancy ($\Delta E = 1.59$ eV). However, in the hypoxic phase of the CO-PROX reaction, the exposed carbon species may be hydrogenated into CH₄ by the abundant H₂ rather than oxidized. Such a minor methanation route is featured by the disparity in the concurrent evolution of CO versus CO₂, which is particularly manifested at high temperatures of the reaction. In our previous work²⁷ we have shown that the extent of the hypoxic methanation over the investigated spinel catalysts does not exceed ~10% of the total CO conversion above 230 °C, in agreement with the literature.^{28,44} It may be then presumed that the extent of the dissociative mechanism of CO oxidation should not exceed this level, and likely is lower in the presence of dioxygen.

In the conceivably simplest scenario of the suprafacial LH/ER mechanism, where adsorbed/gas phase CO is directly

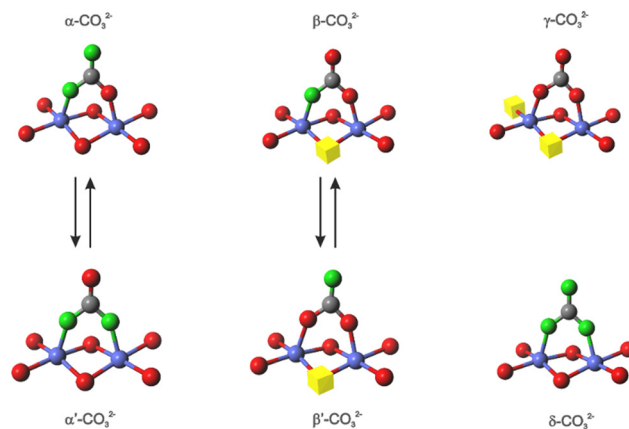


oxidized by adsorbed $^{18}\text{O}_2$ into the corresponding CO_2 isotopomers, the transfer of O-16 from CO into H_2O is not expected, as the CO and H_2 oxidation processes actually have to occur separately, while competing for the scavenging of the $\text{O}_{\text{ads}}/\text{O}_{\text{ads}}$ intermediates only. The resulting isotopic composition with $p_{\%}(\text{H}_2^{18}\text{O}) \gg p_{\%}(\text{H}_2^{16}\text{O})$, thought observed during the sole H_2 oxidation (Fig. 1a), differs drastically from the generic situation with $p_{\%}(\text{H}_2^{16}\text{O}) > p_{\%}(\text{H}_2^{18}\text{O})$ seen in the CO-PROX reaction (Fig. 1c and 2). Thus, such a competitive LH/ER mechanism of direct CO into CO_2 oxidation in parallel to H_2 oxidation cannot constitute a prime route of the investigated CO-PROX process. This is also supported by the disparity in the molar composition of CO_2 predicted by the LH/ER mechanism (2), where $p_{\%}(\text{C}^{16}\text{O}_2) \approx p_{\%}(\text{C}^{18}\text{O}_2)$, and the really observed $p_{\%}(\text{C}^{16}\text{O}_2) > p_{\%}(\text{C}^{18}\text{O}_2)$ relation at low temperatures and $p_{\%}(\text{C}^{16}\text{O}_2) < p_{\%}(\text{C}^{18}\text{O}_2)$ at high temperatures. Notably, the latter behavior provides an indication that the CO-PROX mechanism changes with temperature.

As a result, the interaction of C^{16}O with $^{18}\text{O}_2$ may likely proceed with the formation of the already mentioned surface carbonates as a common intermediate of H_2 oxidation. A facile formation of carbonates and bicarbonate species (identified by the bands located at 1645, 1605, 1545, 1470 and 1437 cm^{-1} (ref. 59–61)) can be inferred from the IR spectra shown in the ESI† along with their detailed interpretation and discussion (chapter S7, Fig. S8a₁₋₂). The development of the surface carbonates during CO oxidation on Co_3O_4 is also well documented in the literature using IR and NAP-XPS techniques.⁵⁷ Hydroxylation of the cobalt spinel surface upon contact with a mixture of H_2 and O_2 and H_2 alone is, in turn, shown by the evolution of hydroxyl bands in the 3700–3300 cm^{-1} region in Fig. S8b₁ and b₂,† respectively. Under the CO-PROX conditions, the carbonate bands are gradually reduced upon contact with H_2 (Fig. S8c₁₋₂,†), which can be attributed to the decomposition of the carbonates *via* bicarbonate and formate species (the bands at 1585 and 1378 cm^{-1} (ref. 62)) into CO_2 (2350 cm^{-1}). The observed changes in the IR spectra indicate a distinct difference in the reactivities toward H_2 of the various surface carbonate/bicarbonate adspecies. As discussed in the ESI† (chapter SX) in more detail, most of the surface carbonates accumulated during the CO-PROX reaction behave as spectator species, as previously proposed based on DFT calculations,⁴¹ and only a small fraction behaves as intermediates.

There are 6 possible types of the carbonate intermediates attached to a pair of the octahedral Co cations ($\text{Co}^{\text{oct}}\text{---}\text{Co}^{\text{oct}}$) located on the (100) surface of the benchmark cobalt spinel, depending on their isotopic composition and the suprafacial or intrafacial mechanism of their formation (Scheme 2). The octahedral cations were selected as primary potential active centers based on the results of the $^{16}\text{O}_2/^{18}\text{O}_2$ isotopic exchange investigations (Fig. S3†), discussed above.

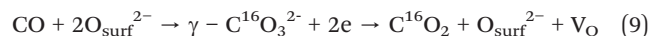
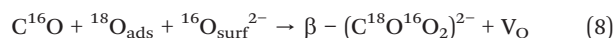
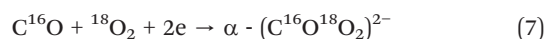
An analogous series can also be conceived for the surface carbonates accommodated on the dual tetrahedral–octahedral, $\text{Co}^{\text{tet}}\text{---}\text{Co}^{\text{oct}}$, cobalt centers (see ESI† Fig. S9), which being much more stable (see below) behave as



Scheme 2 Possible isotopic speciation of the carbonate intermediates, depending on the number of the O-18 labeled atoms, and the suprafacial or intrafacial mechanism of their formation on the $\text{Co}^{\text{oct}}\text{---}\text{Co}^{\text{oct}}$ centers located on the (100) surface of Co_3O_4 . Atom coding: O-16 red, O-18 green, Co blue, C – grey.

spectator species, contributing mostly to the IR spectra shown in Fig. S8.†

In the formation of doubly ($\alpha\text{-CO}_3^{2-}$) and singly ($\beta\text{-CO}_3^{2-}$) ^{18}O -labeled carbonate intermediates, an $^{18}\text{O}_2$ molecule obviously has to be engaged,



alluding to the involvement of the LH/ER ($\alpha\text{-CO}_3^{2-}$) and MvK-LH/ER ($\beta\text{-CO}_3^{2-}$) mechanisms, whereas $\gamma\text{-CO}_3^{2-}$ is produced along the strict MvK pathway, at the expense of only the $^{16}\text{O}_{\text{surf}}^{2-}$ anions (see Fig. S8a₂,†). As already mentioned above, the latter turns into a MvK-LH/ER channel upon dissociative filling of the oxygen vacancy with $^{18}\text{O}_{\text{ads}}$ release, which is next used for oxidation of another CO molecule (see Scheme 1). The relevance of $\delta\text{-CO}_3^{2-}$ should be rather low, when confronting the expected isotopic composition of CO_2 with that actually observed, therefore, this isotopomer will not be taken into account in further mechanistic considerations. Yet, $\gamma\text{-CO}_3^{2-}$ produced under anoxic conditions may be involved in the CO-PROX reaction, as it directly leads to the observed formation of C^{16}O_2 .

Generally, the surface $\text{Co}^{\text{octa}}\text{-CO}_3^{2-}\text{-Co}^{\text{octa}}$ carbonates can be decomposed by rupture of the bridging oxygen bond into carbon dioxide ($\text{CO}_3^{2-} \rightarrow \text{CO}_2 + \text{O}_{\text{ads}}$), with release of $^{18}\text{O}_{\text{ads}}$ or $^{16}\text{O}_{\text{ads}}$ adspecies ($\alpha\text{-CO}_3^{2-}$ and $\beta\text{-CO}_3^{2-}$), ^{18}O ($\alpha'\text{-CO}_3^{2-}$), and ^{16}O adspecies ($\beta'\text{-CO}_3^{2-}$). The bridging oxygen bond can also be broken upon interaction with protons, $\text{CO}_3^{2-} + 2\text{H}^+ \rightarrow \text{CO}_2 + \text{H}_2\text{O}$, produced upon oxidation of H_2 on the catalyst surface. The alternative route of carbonate transformation into CO_2 consists in breaking of the terminal oxygen bond due to the reaction with a gas phase CO or H_2 molecule,



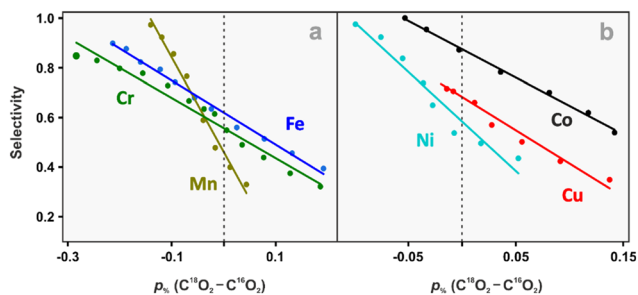
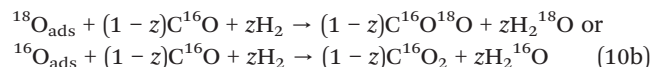
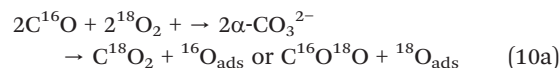


Fig. 6 Correlation between the selectivity and the relative content of $C^{18}O_2$ and $C^{16}O_2$ in the CO-PROX reaction for the B-type (a) and A-type (b) spinel catalysts, displayed separately for the better clarity.

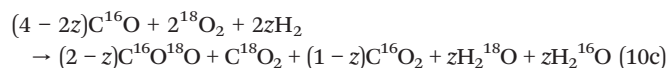
which implies the operation of an ER step (see Fig. S8c₂ and c₃†). The intermingling of CO and H₂ oxidation during the CO-PROX reaction is well supported by a remarkable correlation between the catalyst selectivity and the difference in the relative content of $C^{18}O_2$ and $C^{16}O_2$ in the reaction products (Fig. 6), which in our isotopic analysis is regarded as a crucial empirical constraint for the establishment of the generic reaction mechanism. The slopes of the lines depend on the type of the dopant, and the observed differences may largely be traced back to the contribution of H₂ oxidation to the selectivity beyond the carbonate/bicarbonate mechanism, as explained in more detail below.

The conceivable patterns of the isotopically resolved transformations of the carbonate intermediates into CO₂ and H₂O in the presence of the hydrogen and carbon monoxide reactants are summarized in Fig. 7, for the α -CO₃²⁻ and α' -CO₃²⁻ intermediates, taken as an example. For the remaining carbonates, the analogous patterns are collated in Fig. S10 and S11.†

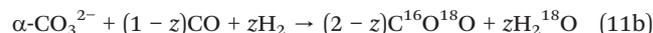
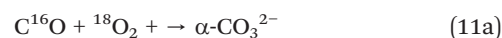
For the α -CO₃²⁻ pathway, when the O_{ads} intermediates are scavenged by CO and H₂, neglecting the CO₂ scrambling and the isotopic exchange with the surface (see Fig. 3a and b), the suprafacial LH/ER- α_1 mechanism based on the bridging oxygen dissociation (see the corresponding shaded fragments in Fig. 7a) can concisely be formulated as



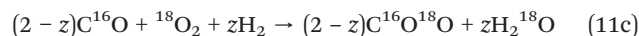
which in total leads to



In the case of the terminal oxygen involvement, the ensuing Eley-Rideal oxidation of CO (Fig. 7a₁) or H₂ (Fig. 7a₂) will overall proceed along the following route



yielding



Such an alternative of the suprafacial mechanism will be labeled as LH/ER- α_2 . For the α' -CO₃²⁻ species (Fig. 7b-b₂), the resulting equations, derived in an analogous way, assume the form

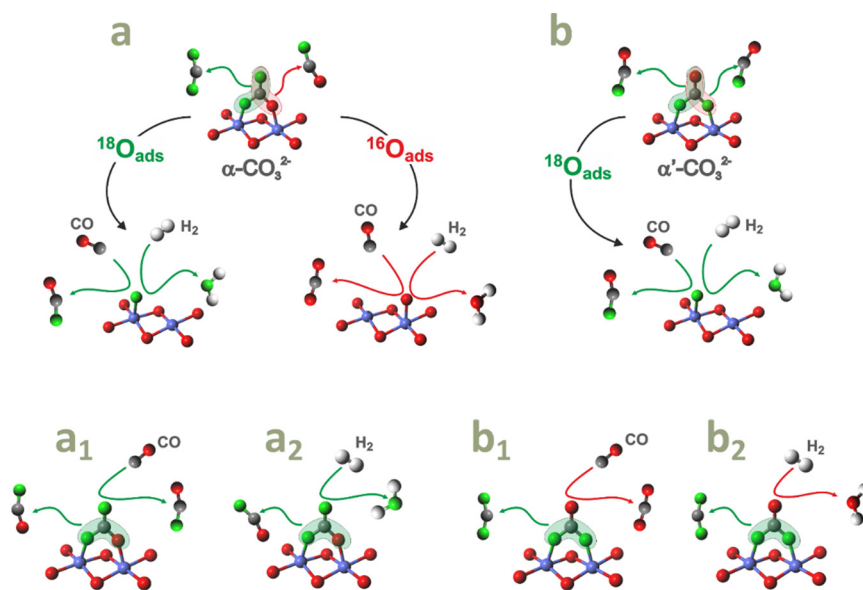
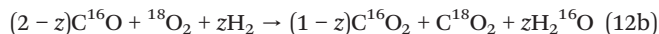
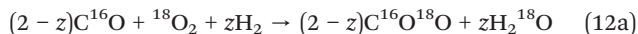


Fig. 7 Possible pathways of transformation of the surface α -CO₃²⁻ (a) and α' -CO₃²⁻ intermediates (b) into the CO₂ and H₂O isotopomers in the presence of the CO (a₁ and b₁) and H₂ reactants (a₂ and b₂).

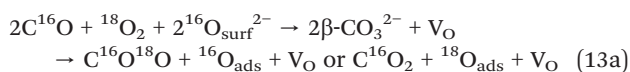




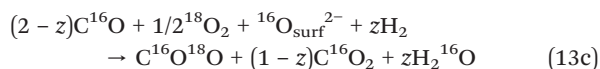
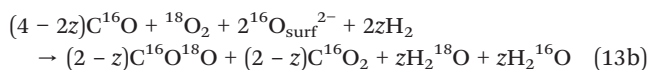
constituting the mechanistic LH/ER- α'_1 and α'_2 variants of the suprafacial CO-PROX reaction.

It should be emphasized that in the proposed scenario, all the isotopic products, namely $\text{C}^{16}\text{O}^{18}\text{O}$, C^{18}O_2 , C^{16}O_2 , H_2^{18}O and H_2^{16}O , are explicitly produced, in qualitative accordance with the experimental results. However, since their relative abundances are not congruent with those seen actually in the isotopic studies (Fig. 4 and 5), this scheme, while being hypothetically most relevant, is certainly not operating alone.

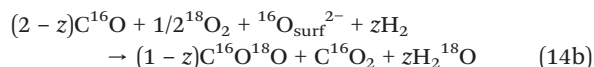
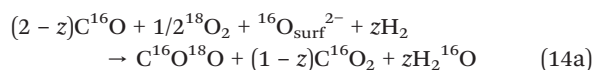
In the case of the $\beta\text{-CO}_3^{2-}$ pathway, the surface carbonates are produced with participation of the lattice and gas phase oxygen (see Fig. S10a- a_2^\dagger)



Subsequent scavenging of the resultant $^{16}\text{O}_{\text{ads}}$ or $^{18}\text{O}_{\text{ads}}$ adspecies by gaseous CO and H_2 occurs in the same way as for $\alpha\text{-CO}_3^{2-}$ (eqn (10b)), leading in total to the development of the following intrafacial MvK-LH/ER- β_1 and β_2 reactions,



The corresponding equations for the $\beta'\text{-CO}_3^{2-}$ intermediates (Fig. S10b- b_2^\dagger) may be written as

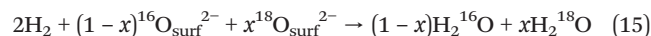


for the MvK-LH/ER- β'_1 and β'_2 pathways, respectively. In this case, the appearance of C^{18}O_2 is not expected, and both water isotopomers are formed along different variants of the $\beta'\text{-CO}_3^{2-}$ transformation. Finally, only C^{16}O_2 species are produced *via* the MvK mechanism through the $\gamma\text{-CO}_3^{2-}$ adspecies.

Summarizing, in the case of the $\alpha\text{-CO}_3^{2-}$ and $\alpha'\text{-CO}_3^{2-}$ intermediates, the LH/ER- α_1 mechanism leads to $p_{\%}(\text{C}^{16}\text{O}^{18}\text{O}) \geq p_{\%}(\text{C}^{18}\text{O}_2) \geq p_{\%}(\text{C}^{16}\text{O}_2)$, and the ratio of $\text{H}_2^{16}\text{O}/\text{H}_2^{18}\text{O} = 1$. The LH/ER- α'_1 and LH/ER- α_2 schemes of the same isotopic composition, with $\text{C}^{16}\text{O}^{18}\text{O}$ and H_2^{18}O as the only products, cannot be distinguished. The LH/ER- α'_2 route, in turn, is characterized by the lack of $\text{C}^{16}\text{O}^{18}\text{O}$ and H_2^{18}O , and $p_{\%}(\text{C}^{18}\text{O}_2) > p_{\%}(\text{C}^{16}\text{O}_2)$. When the $\beta\text{-CO}_3^{2-}$ and $\beta'\text{-CO}_3^{2-}$ intermediates are involved, C^{18}O_2 is always absent, and the contributions of C^{16}O_2 and H_2^{16}O are enhanced. This is particularly important for proper reproduction of the isotopic

composition in the low and medium temperature stages of the CO-PROX species. The MvK-LH/ER- β_2 and β'_1 pathways give rise to the same products (so they again are indistinguishable), with high abundance of C^{16}O_2 and H_2^{16}O . For the MvK-LH/ER- β_1 scheme, $p_{\%}(\text{C}^{16}\text{O}^{18}\text{O}) = p_{\%}(\text{C}^{16}\text{O}_2)$ and $p_{\%}(\text{H}_2^{16}\text{O}) = p_{\%}(\text{H}_2^{18}\text{O})$. Application of these constraints allows for recognition of the main type of mechanism operating in the CO-PROX reaction in the particular temperature window. Evidently, none of the possible mechanisms discussed herein can be reconciled with the experimental data directly. However, the observed isotopic composition profiles can be accounted for by involvement of the carbonate $\alpha\text{-CO}_3^{2-}$ and $\beta/\beta'\text{-CO}_3^{2-}$ intermediates, and the corresponding combination of the suprafacial and intrafacial mechanisms, quite fairly.

The already mentioned pathways of parallel H_2 oxidation by $^{18}\text{O}_2$ may occur along the direct LH route (as in for sole H_2 oxidation, see eqn (1)) or its intrafacial option,



which is illustrated in Fig. 1a and S8b $_{1,\dagger}$ where the associated surface hydroxylation is confirmed by the IR spectra. Hydrogen may also be activated *via* the electroprotic pathway (EP) with the formation of surface hydroxyls, and the released electrons are accommodated in the metal 3d band, the feasibility of which is documented by IR in Fig. S8b $_{2,\dagger}$



This pathway is favored by the basicity of surface $\text{O}_{\text{surf}}^{2-}$ anions. In the case of Co_3O_4 , it faces a barrier of 1.11 eV,⁵² implying its growing importance in the high temperature stage of the CO-PROX reaction, where the gas phase dioxygen becomes depleted. The resulting surface protons (present in the form of hydroxyl groups, see Fig. S8b $_{2,\dagger}$) can easily diffuse on the catalyst surface, and participate in the transformation of the carbonate intermediates into bicarbonate and then into CO_2 and H_2O , as shown in Fig. S8c $_{2,\dagger}$ and previously proposed for copper oxide-cerium oxide catalysts.⁶³ Such a process contributes thus to the decrease in catalyst selectivity, which is especially important in the hypoxic stage of the CO-PROX reaction (Fig. S4c $_{\dagger}$).

The isotopic composition observed during the sole H_2 oxidation (Fig. 1a) disfavors the dominant involvement of the Mars van Krevelen related mechanisms, in agreement with the relatively high energy barrier of 1.71 eV for the intrafacial extraction of H_2O . The LH/ER mechanism, in turn, explains well the fact that $p_{\%}(\text{H}_2^{18}\text{O}) \gg p_{\%}(\text{H}_2^{16}\text{O})$, seen in Fig. 1a for the oxidation of H_2 alone. However, a quick inspection of Fig. 1c, where $p_{\%}(\text{H}_2^{16}\text{O}) > p_{\%}(\text{H}_2^{18}\text{O})$, demonstrates undoubtedly that the suprafacial LH/ER mechanism cannot be directly extended into H_2 oxidation during the CO-PROX reaction, in agreement with the postulated participation of hydrogen in the carbonate mechanism of CO oxidation, discussed above.



The isotopic composition for the **B**-type catalysts (Cr–Co, Mn–Co and Fe–Co) shows a characteristic pattern with $p_{\%}(\text{C}^{16}\text{O}^{18}\text{O}) \approx 0.5 > p_{\%}(\text{C}^{16}\text{O}_2) \gg p_{\%}(\text{C}^{18}\text{O}_2)$ at low temperatures, which changes into $p_{\%}(\text{C}^{16}\text{O}^{18}\text{O}) > p_{\%}(\text{C}^{18}\text{O}_2) > p_{\%}(\text{C}^{16}\text{O}_2)$ at high temperatures, (Fig. 5a–c), where the selectivity significantly drops (Fig. S4c†). In parallel, $p_{\%}(\text{H}_2^{16}\text{O}) > p_{\%}(\text{H}_2^{18}\text{O})$, and the discrepancy in the content of both water isotopomers generally decreases with increasing temperature. The $\delta_{16}(\text{CO}_2)$ parameter assumes its higher values at the beginning, and then drops below the reference value of 0.515 due to the simultaneous H_2 oxidation and transfer of O-16 to water. Such behavior can be accounted for by the co-operation of the suprafacial LH/ER- α_1 and the intrafacial MvK–LH/ER- β_2/β'_1 mechanisms. The involvement of the latter is characterized by the high content of C^{16}O_2 and H^{16}O and $\delta_{16}(\text{CO}_2) > 0.515$ in the first phase of the CO-PROX reaction, whereas transition from the C^{16}O_2 to C^{18}O_2 dominance with the temperature (second phase of the reaction) is diagnostic of enhanced H_2 oxidation. Extinction of O_2 with the reaction progress triggers the EP route of H_2 activation, and the $\delta_{16}(\text{CO}_2)$ values fall well below 0.515. The ensuing domination of C^{18}O_2 over C^{16}O_2 results from the trade-off between the CO and H_2 reactants for the scavenging of O_{ads} , as predicted by the LH/ER- α_1 pathway. Within this model, the growing divergence between the C^{18}O_2 and C^{16}O_2 contents is correlated with the loss of the catalyst selectivity (see Fig. 6a). Indeed, it is noticeably larger for the Cr–Co and Fe–Co catalysts than for the more selective Mn–Co spinel, in the mid-temperature range.

Among the **A**-type spinels, for the bare Co_3O_4 (Fig. 4b) and Ni–Co catalysts (Fig. 5d), the isotopic composition pattern is qualitatively similar to that observed for the **B**-type spinels, suggesting that the gross mechanistic features of the CO-PROX reaction are essentially akin. However, the performance of the Cu–Co (Fig. 5e) and Zn–Co (Fig. 5f) mixed spinels shows clearly a more distinct character. The isotopic composition for Cu–Co in the wide temperature range exhibits a unique $\text{C}^{16}\text{O}^{18}\text{O}/\text{C}^{18}\text{O}_2/\text{C}^{16}\text{O}_2$ ratio of 2:1:1, with the $p_{\%}(\text{C}^{18}\text{O}_2)$ vs. $p_{\%}(\text{C}^{16}\text{O}_2)$ divergence beginning already above 200 °C. Furthermore, the $\delta_{16}(\text{CO}_2)$ parameter until 200 °C is very close to 0.515, indicating that the lattice oxygen is not significantly transferred to CO_2 . This behavior can be explained by the dominant suprafacial LH/ER- α_1 mechanism operating until 200 °C, with delayed H_2 oxidation. The related loss of the Cu–Co spinel selectivity in the late stage of the reaction (see Fig. S4c†) leads to the corresponding drop of $\delta_{16}(\text{CO}_2)$ below 0.515. The MvK–LH/ER- β_2/β'_1 contribution to the CO and H_2 oxidation is less important in this case. The unique behavior of the Zn–Co catalyst is highlighted by $p_{\%}(\text{C}^{18}\text{O}_2) > p_{\%}(\text{C}^{16}\text{O}_2)$ and $\delta_{16}(\text{CO}_2) < 0.515$ in the whole temperature range. Such an isotopic pattern of the carbon dioxide can be explained rather easily in terms of an early H_2 oxidation already at low temperatures (in contrast to Cu–Co), which agrees well with the remarkably low selectivity of this catalyst (Fig. S4c†). The isotopic composition of carbon dioxide as well as $p_{\%}(\text{H}_2^{18}\text{O}) \approx p_{\%}(\text{H}_2^{16}\text{O})$ is in line with the prime operation of the LH/ER- α_1 mechanism.

The initial deviations of $\delta_{16}(\text{CO}_2)$ from the reference value are more pronounced for the **B**-type catalysts than for the **A**-type ones, which indicates an enhanced contribution of the MvK–LH/ER mechanism in the former case. This finding may be traced back to the larger lattice constant of the **B**-type spinels (see Table S1†), which lowers the electrostatic stabilization of the $\text{O}_{\text{surf}}^{2-}$ anions by decreasing the Madelung energy, which is beneficial for their catalytic availability in the Mars van Krevelen step.

In order to substantiate the qualitative analysis described above, using eqn (10)–(14) we performed simulations of the development of CO_2 and H_2O isotopomers in the course of the CO-PROX reaction (expressed as a molar isotopic composition, calculated separately for CO_2 and H_2) as a function of the z parameter (taken as an independent variable), for the selected catalyst (Co_3O_4 , $\text{Co}_3^{18}\text{O}_4$, Fe–Co, and Ni–Co) that represents each of the spinel **A** and **B** types. The simulations were based on the operation of a mixed mechanism involving the suprafacial and intrafacial oxidation routes. Among the examined possible reaction combinations described in eqn (10)–(14), the simulated results that are closest to the experimental data were obtained for the concurrent operation of the suprafacial LH/ER- α_1 and intrafacial MvK–LH/ER- β_2/β'_1 pathways (the latter two are isotopically indistinguishable). The obtained isotopic composition profiles are plotted as a function of z (Fig. 8a₁–d₁), with the superimposed experimental values obtained upon translation of the temperature dependence of the experimental selectivity (Fig. S4c†) into the corresponding values of z with the points taken in steps of 10 °C. However, because hydrogen may also be oxidized independently of the carbonate pathway, the positions of the experimental points correspond approximately to the z values used in the simulations. The latter are limited to the theoretical selectivity of 0.5 when $z = 1$, as implied by the carbonate-mediated CO-PROX reaction model. Thus, the experimental selectivities less than 0.5 indicate that, in addition to the carbonate pathway, hydrogen is also oxidized along a parallel route. A fairly good proximity of the predicted patterns of CO_2 isotopic composition with the experiment for bare Co_3O_4 (Fig. 8a₁) and Co^{18}O_4 (Fig. 8b₁) as well as for **B**-type Fe–Co (Fig. 8c₁) and **A**-type Ni–Co (Fig. 8d₁), can be regarded as a decent roughly-quantitative corroboration of the proposed analysis of the mechanism, performed on the basis of the isotopic composition of the CO-PROX reaction products. However, a distinct deviation of the predicted C^{16}O_2 profiles in the higher temperature region remains significant. Further improvement in the matching degree with the experiment was achieved by adding C^{16}O_2 to the reaction products (Fig. 8a₂–d₂). It implies that apart from the carbonate cycle already considered, CO_2 may also be produced through direct MvK oxidation of CO or possibly *via* $\gamma\text{-CO}_3^{2-}$ intermediates (at the extent varying from 0.15 to 0.22), with the exception of Cu–Co and Zn–Co where this pathway is not engaged. The contribution of the suprafacial mechanism tends to be significantly lower for the **B**-type spinels (0.37–0.56) than for the **A**-type spinels (0.56–



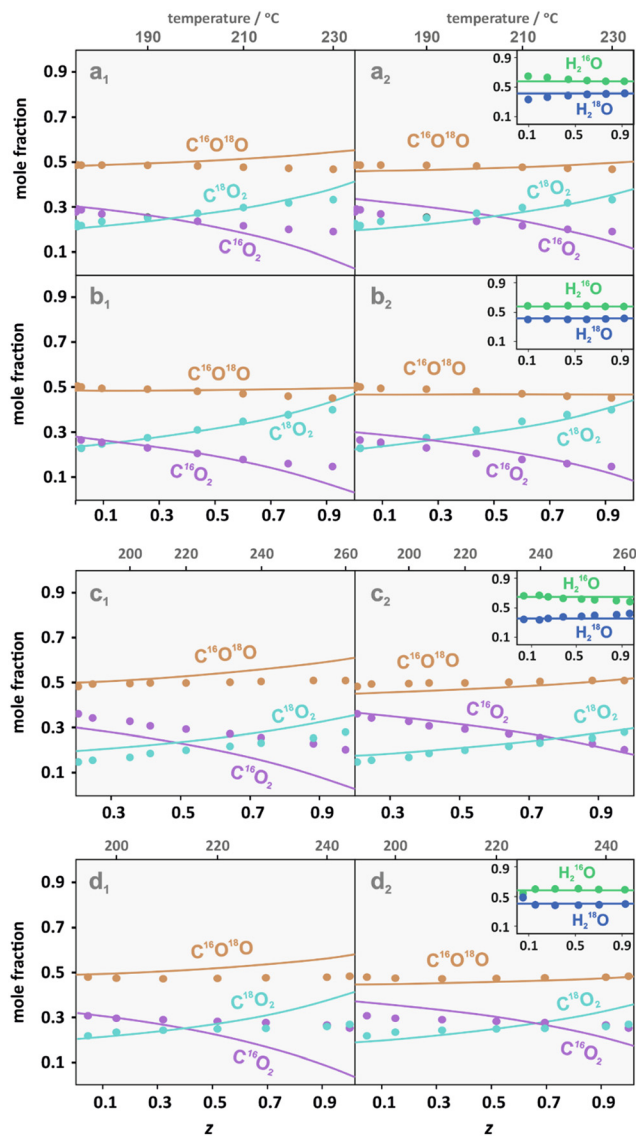


Fig. 8 Isotopic mole fraction profiles (solid lines) plotted as a function of the z parameter based on the combination of the mechanism described by eqn (10c) and (14a) with (a₁–d₁) and without (a₂–d₂) additional contribution of C¹⁶O₂. The corresponding results for the H₂O isotopomers are shown in the inserts. The dots refer to the experimental isotopic composition for the z values calculated from the selectivity. Catalyst coding: Co₃O₄ – a₁, and a₂; Co₃¹⁸O₄ – b₁, and b₂; Fe–Co – c₁, and c₂; Ni–Co – d₁, and d₂.

0.83), in agreement with the changes in the $\delta_{16}(\text{CO}_2)$ values. Another confirmation of the proposed mechanism of the CO-PROX reaction is provided by the fact that the molar composition of the CO₂ isotopomers can be well reproduced for the Co₃¹⁶O₄ and Co₃¹⁸O₄ spinels within the same combination of the suprafacial and intrafacial mechanisms, and only the isotopic labeling of the catalyst changed accordingly (Fig. 8a₂ and b₂). The analysis is also validated by proper reproduction of the $p_{\%}(\text{H}_2^{16}\text{O})$ and $p_{\%}(\text{H}_2^{18}\text{O})$ contributions for all types of the investigated catalysts (Fig. 8 inserts), using the relative involvement of the LH/ER- α_1 and MvK-LH/ER- β_2/β_1' pathways established after matching

the molar composition of the CO₂ isotopomers only. Finally, the “experimental” $z > 1$ clearly indicates that part of hydrogen is oxidized along the parallel routes described in eqn (15) and (16), which are especially important in the case of the A-type catalysts, and for the Zn–Co spinel in particular. In this case, the CO-PROX reaction proceeds *via* the combination of the LH/ER- α_1 (0.83) and MvK-LH- β' (0.17) pathways, with parallel oxidation of H₂, but without direct CO oxidation by lattice oxygen. The corresponding simulation of the CO₂ and H₂O isotopic profiles is shown in Fig. S12a.†

Inspection of Fig. 5 indicates that significant deviation from the generic composition pattern, $p_{\%}(\text{C}^{16}\text{O}^{18}\text{O}) > p_{\%}(\text{C}^{16}\text{O}_2) > p_{\%}(\text{C}^{18}\text{O}_2)$ with the reversal of the C¹⁶O₂ and C¹⁸O₂ content at higher temperatures, occurs for the Cu–Co catalyst (Fig. 5e). The fact that $p_{\%}(\text{C}^{16}\text{O}^{18}\text{O}) > p_{\%}(\text{C}^{16}\text{O}_2) \approx p_{\%}(\text{C}^{18}\text{O}_2)$ until 210 °C can be explained by the predominant operation of the LH/ER- α_1 mechanism (0.69) with a persistently small value of the z parameter in this temperature window. The observed lower selectivity in comparison to the carbonate model prediction, leading to the corresponding larger “experimental” z -values, may probably be associated with an enhanced hydrogen oxidation (see eqn (15) and (16)) on the segregated CuO phase of the significant 17.7% abundance (see Table S1†). Indeed, the apparent activation energy of 14.5 kcal mol^{−1} for the EP oxidation is favorable for the occurrence of this reaction,⁶⁴ and full conversion of H₂ oxidation was actually observed for CuO below 250 °C in a separate measurement. The subsequent growing deviation between $p_{\%}(\text{C}^{16}\text{O}_2)$ and $p_{\%}(\text{C}^{18}\text{O}_2)$ above 210 °C can be accounted for quite easily by the gradual development of the H₂ oxidation *via* the carbonate intermediates. The resulting simulation of the corresponding CO₂ and H₂O isotopic profiles shown in Fig. S12b,† upon adjusting the z -scale to the observed selectivity purposely, remains again in good agreement with the experiment.

Summarizing, the thorough analysis of the isotopically resolved reaction products shows clearly that only by invoking the cooperation of the suprafacial (LH/ER- α_1) and intrafacial (MvK-LH/ER- β_2/β_1') mechanisms based on carbonate intermediates, with inclusion of the possibility of parallel direct oxidation of CO and H₂, can we explain the simultaneous appearance of all C¹⁶O₂, C¹⁸O₂, C¹⁶O¹⁸O, H₂¹⁸O and H₂¹⁶O products in proportions fairly compatible with the experimental results, $p_{\%}(\text{C}^{16}\text{O}^{18}\text{O}) \geq p_{\%}(\text{C}^{16}\text{O}) \geq p_{\%}(\text{C}^{18}\text{O})$, and $p_{\%}(\text{H}_2^{16}\text{O}) > p_{\%}(\text{H}_2^{18}\text{O})$, including also the particular features of the Cu–Co and Zn–Co catalyst, with $p_{\%}(\text{C}^{16}\text{O}^{18}\text{O}) \approx 2p_{\%}(\text{C}^{16}\text{O}) \approx 2p_{\%}(\text{C}^{18}\text{O})$ and $p_{\%}(\text{C}^{18}\text{O}) \geq p_{\%}(\text{C}^{16}\text{O})$, $p_{\%}(\text{H}_2^{18}\text{O}) \approx p_{\%}(\text{H}_2^{16}\text{O})$, respectively. The specific behavior of the latter catalysts is characterized also by enhanced H₂ oxidation and virtually suppressed direct MvK oxidation of CO into CO₂.

It should be emphasized, however, that the proposed heuristic approach provides a semiquantitative mechanistic account only. It may be next substantiated by performing more comprehensive mechanistic investigations with SSITKA-DRIFTS techniques or rigorous isothermal microkinetic modeling based on material balance.^{65,66} Nonetheless, the



intricate nature of the CO-PROX reaction mechanism, involving operation of the intrafacial and suprafacial pathways, as well as the pivotal role of the carbonate intermediates was definitely established.

3.4. Molecular modelling and first principles thermodynamic account

Within the context of the proposed mechanism, the formation and thermal stabilities of the surface CO, O₂, carbonate and hydroxyl adspecies play a vital role in the molecular understanding of the sustainable turnover of the CO-PROX process, and the overall behavior of the spinel catalysts. We addressed this issue preliminarily by *ab initio* thermodynamic and molecular DFT modeling performed for the (100) surface of the parent Co₃O₄ spinel (see TEM results in Fig. S2†), as a representative example. To evaluate the formation and stability of these intermediates under various thermodynamic conditions (the reaction temperature and the pressure of CO, O₂, H₂, CO₂ and H₂O), we constructed the corresponding 3D thermodynamic diagram shown in Fig. 9a, using the DFT energies collated in Table S2† (with the epitomized structures presented in Fig. S13†). The

corresponding 2D bottom projection for the adsorbed O₂ and CO species (with carbonate formation excluded) was obtained by assuming $p_{\text{CO}} = p_{\text{O}_2}$, since both pressures change in the same fashion as the progress of the CO-PROX reaction (Fig. 9b). This thermodynamic diagram reveals the conditions of CO and O₂ adsorption at the Co^{tet} and Co^{oct} sites, and the surface stability of the corresponding adducts, which appear to depend more strongly on the temperature than the reactant pressure. In the temperature window of the CO-PROX reaction, the surface is covered preferentially by diatomic and monoatomic reactive oxygen species, providing the requisite playground for the occurrence of the suprafacial LH/ER mechanism, proposed upon conceptualization of the isotopic studies. Furthermore, analysis of the thermodynamic surface stability of the O₂ and CO adspecies (see Fig. S14†) suggests that the LH pathway should gradually evolve into the ER one with increasing temperature of the CO-PROX reaction, justifying the applied merging of both schemes into a more general suprafacial LE/ER mechanism, for the sake of the conciseness.

The surface carboxylation and hydroxylation thermodynamics is shown in the relevant 2D diagrams in Fig. 9c and d, which illustrate how these key processes are

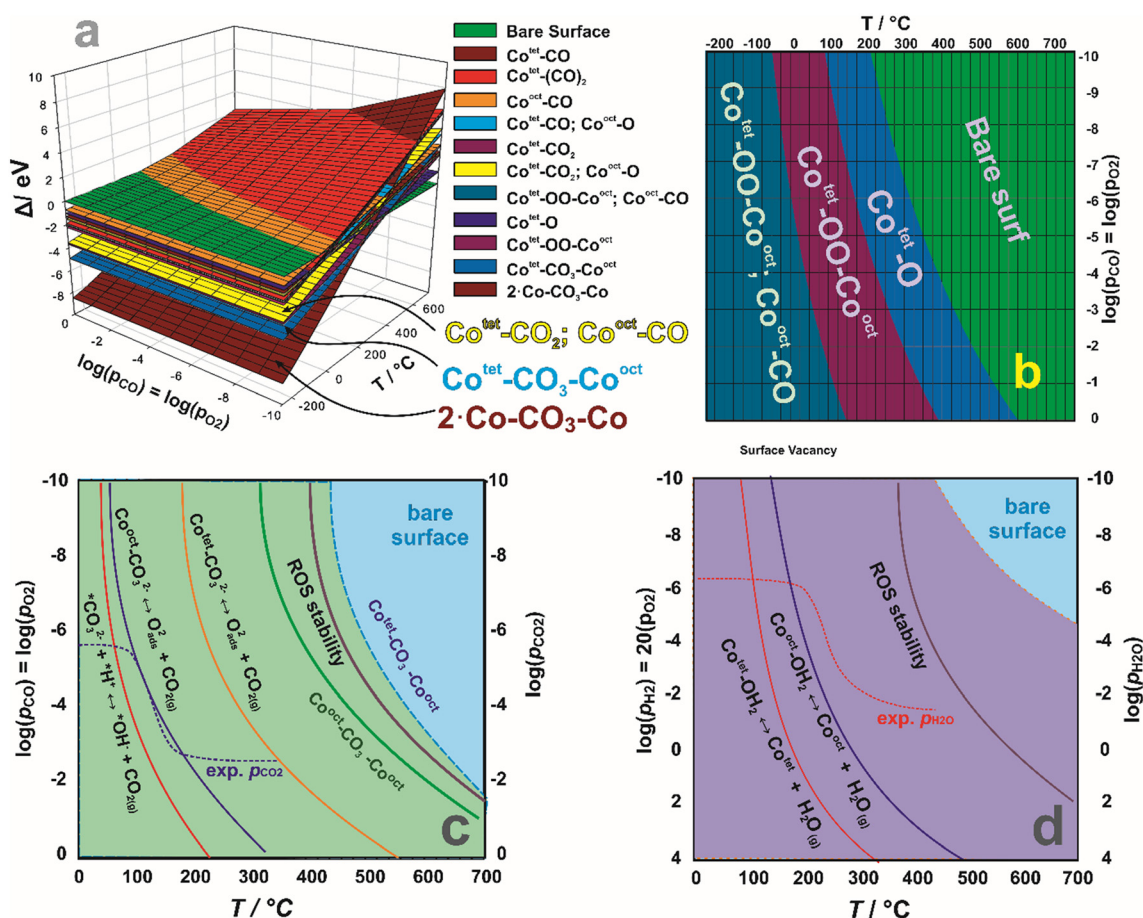


Fig. 9 Perspective view of the thermodynamic 3-dimensional (ΔE , T , p) diagrams showing the relative stability of all relevant oxygen, carbonyl, carbonate and hydroxyl intermediates (a) together with its 2D bottom projection for the adsorbed O₂ and CO species (with carbonate forms excluded) (b). In the bottom part thermodynamic diagrams of surface carboxylation (c) and hydroxylation (d) are shown.



controlled by the reaction conditions. The mechanistically most important implication for the CO-PROX reaction is the fact that the oxidation of CO into the surface carbonates is definitely more favored over the direct oxidation into CO₂, as it can be inferred from the relative position of the corresponding thermodynamic stability planes (marked in yellow, blue and brown in Fig. 9a).

The thermodynamic boundary of surface carbonate formation from O₂ and CO is indicated by the blue dashed line in Fig. 9c. The large green area completely covers the range of the temperature and O₂ or CO pressure variations during the CO-PROX reaction, defining the thermodynamic incentive for the formation of surface carbonates. The carbonate intermediates can decompose into CO₂ and O_{ads} at much lower temperatures (delineated by the solid dark blue and orange lines for the carbonates stabilized at the Co^{tet} and Co^{oct} centers, respectively) than back into the CO and O₂ reactants (shown by the solid green and dotted blue lines). The latter, if treated as a reference of the carbonate energetic stability, may lead to misleading conclusions regarding their role in the CO-PROX reaction. As implied by the experimental changes of the CO₂ pressure during the reaction, superimposed on the diagram, the decomposition of the carbonates that are accommodated on the dual Co^{oct}–Co^{oct} centers into CO₂ and O_{ads} species may already begin around 150 °C. The resulting CO₂ molecules are completely released well below 100 °C, due to the low binding energy, $E = -0.42$ eV, for this process (see Table S2 and Fig. S15† for more details), in nice agreement with the experimental lack of CO₂ retention (Fig. S6†).

In this temperature range, the surface Co^{oct}–CO₃²⁻–Co^{oct} carbonates may also be decomposed along an even more efficient protonation pathway (CO₃²⁻ + 2H⁺ → CO₂ + H₂O), see the solid red line in Fig. 9c. Operation of this route is controlled by availability of itinerant H⁺ species, the formation of which being more demanding than direct LH/ER oxidation by oxygen adspecies which is favored at higher temperatures, as manifested by the pronounced decrease in the selectivity above 200–220 °C. The barrier of the electroprotic H₂ dissociation being equal to 1.11 eV for cobalt spinel, decreasing down to 0.78 eV for Zn–Co, together with the more favorable reaction energetics (–1.14 eV vs. –2.11 eV, respectively, see Fig. S16†), explains well the distinctly lower selectivity of the Zn–Co catalyst compared to Co₃O₄. In the case of carbonates attached to the dual Co^{tet}–Co^{oct} centers, the energy of their dissociation into CO_{2(g)} ($\Delta E = 1.29$ eV) is substantially higher than that for the Co^{oct}–Co^{oct} pairs ($\Delta E = 0.69$ eV), which is reflected in the much higher temperature ($T > 300$ °C, for $p_{\text{CO}_2} = 0.01$ atm) of the CO₂ release from these centers (orange line). As a result, such adspecies behave as spectators that being accumulated during the CO-PROX reaction are primarily observed in the IR spectra (see Fig. S8†), but are rather of minor importance for the CO-PROX reaction, resolving the contradictory claims about the mechanistic role of carbonates found in the literature.^{41,57}

An analogous diagram was constructed for suprafacial H₂ oxidation, setting $p_{\text{H}_2} = 10p_{\text{O}_2}$ (Fig. 9d). The purple area delineates the region of thermodynamic conditions that are favorable for the production of hydroxyl groups due to H₂ oxidation. For $p_{\text{H}_2\text{O}} \sim 10^{-2}$ atm, the surface dehydroxylation occurs around 250 and 150 °C, depending on the topographic location of the hydroxyl groups (on the Co^T or Co^O cations). These results indicate that during the CO-PROX reaction, partial hydroxylation of the catalyst surface is thermodynamically favorable below 200 °C, which may lead to loss of the active sites, particularly relevant for the catalysts of lower selectivity in this temperature region (B-type spinels). However, a more efficient channel of hydroxyl removal consists in their participation in the transformation of carbonates into bicarbonates, which then readily decompose into CO₂ and H₂O (Fig. 9c and S8c2†).

Furthermore, the auxiliary theoretical simulations of water desorption from the cobalt spinel surface (see Fig. S17 and the corresponding more detailed discussion in section S15 in the ESI†) confirm that that water adsorption/desorption phenomena should not affect the isotopic composition of H₂O.

The thermodynamic provisions for the operation of the Mars van Krevelen mechanism are shown in Fig. 10, where the free enthalpies (ΔG_r) of the crucial reactions of CO (dotted red line) and H₂ (dotted green line) oxidation by lattice oxygen, and refilling of the resulting oxygen vacancies by O₂ (dotted black line) are plotted against temperature. All processes are thermodynamically strongly favorable throughout the temperature range of the CO-PROX reaction (marked in yellow), indicating that the vacancies produced by CO and H₂ can easily be healed by dioxygen. However, the activation barriers for CO and H₂ oxidation by O_{surf}²⁻ anions differ significantly (0.4 and 0.71 eV, respectively), implying that the MvK oxidation of CO is kinetically more favorable in the CO-PROX temperature window, in agreement with the experimental findings (see Fig. 8). For the oxygen pressure of $p_{\text{O}_2} = 10^{-2}$ atm present in the early stage of the PROX reaction, the ΔG_r value of the oxygen vacancy refilling (dashed black line) changes its sign above ~430 °C. Thus, in the whole PROX temperature window, the MvK mechanism may thermodynamically be maintained. However, in the late stages of the CO-PROX reaction when the oxygen pressure drops below 10⁻⁵ atm (hypoxic conditions represented by the

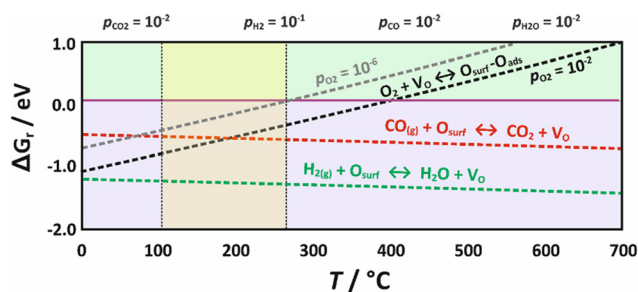


Fig. 10 Thermodynamic analysis of the Mars van Krevelen oxidation of CO and H₂.



dashed grey line), this threshold falls below 270 °C, which means that under such conditions the spinel catalyst starts to be gradually reduced. The MvK catalytic cycles cannot be readily closed by restoring the O_{surf}^{2-} species with gaseous dioxygen, and the CO-PROX reaction turns into a mere H_2 -TPR process.

The essential features of the proposed mutable mechanism of CO-PROX are epitomized by a functional model shown in Fig. 11. It illustrates the three main catalytic cycles distinguished in the CO-PROX reaction, the relative participation of which depends on the catalyst nature and the reaction conditions. Cycle I refers to the indirect CO oxidation *via* suprafacial $\alpha\text{-CO}_3^{2-}$ and intrafacial $\beta\text{-CO}_3^{2-}$ intermediates (LH/ER and MvK-LH/ER), cycle II to direct CO oxidation into CO_2 by lattice oxygen (MvK), while cycle III to direct H_2 oxidation preferably by adsorbed oxygen (LH/ER or EP). The identified diagnostic features for cycle I include the transfer of O-16 from CO to $H_2^{16}\text{O}$, the formation of C^{18}O_2 at the expense of C^{16}O_2 , and $p(H_2^{16}\text{O}) > p(H_2^{18}\text{O})$ when $^{18}\text{O}_2$ is used as an oxidant. Cycle II is characterized by the development of C^{16}O_2 at the expense of $\text{C}^{16}\text{O}^{18}\text{O}$, whereas cycle III by the selectivity drop below the carbonate limit.

The relevance of the distinguished mechanistic pathways changes with increasing temperature and the associated evolution of reaction conditions from oxic to hypoxic, which primarily controls the relative involvement of O_{ads} and O_{surf}^{2-} reactive oxygen species in CO and H_2 oxidation. Although the catalyst surface becomes carboxylated due to the accumulation of spectator CO_3^{2-} adspecies, the CO-PROX reaction can be efficiently facilitated by the minor carbonate intermediates produced along the LH/ER or MvK-LH/ER

pathways (cycle I) over the dual $\text{Co}^{\text{oct}}\text{---}\text{Co}^{\text{oct}}$ sites (in the case of the parent Co_3O_4 catalyst), resolving the conundrum of the mechanistic role of surface carbonates. Hydrogen is partly oxidized by O_{ads} intermediates released upon $\text{Co}^{\text{oct}}\text{---}\text{CO}_3^{2-}\text{---}\text{Co}^{\text{oct}}$ decarboxylation. With decreasing dioxygen concentration, enhanced oxidation of hydrogen occurs in parallel *via* an electroprotic (EP) process (cycle III – orange circle), favored over the A-type spinels. Once anoxic conditions are achieved, the catalyst surface is reduced due to lattice oxygen extraction by H_2 and subsequent $H_2\text{O}$ desorption, and the CO-PROX reaction turns into a mere H_2 -TPR. The CO oxidation capacity of the spinel catalysts benefits from the facile reduction and reoxidation of the octahedral cations. The resulting effective electron sink and source centers are capable of harboring the excess electrons left upon CO_2 formation, until they are used for the intra- and suprafacial O_2 activation processes. The diagnostic features of cycle I, when $^{18}\text{O}_2$ is used as an oxidant, consist of transfer of O-16 from CO to $H_2^{16}\text{O}$, formation of C^{18}O_2 at the expense of C^{16}O_2 and higher contribution of $H_2^{16}\text{O}$ than $H_2^{18}\text{O}$.

Conclusions

It was shown that only when the suprafacial (LH/ER) and intrafacial (MvK) mechanisms operate concurrently can the predicted results be reconciled with the experimental isotopic compositions of CO_2 and $H_2\text{O}$, and their evolution with the progression of the CO-PROX reaction over the examined spinel catalysts. Two types of carbonate adspecies, acting as reaction intermediates (inferred from isotopic composition) or spectators (revealed by IR), were distinguished, and their surface binding topologies were established. The suprafacial LH/ER mechanism consists of CO oxidation into surface carbonates (primary key intermediates), and triggers competitive oxidation of CO *versus* H_2 by the monatomic oxygen species (secondary intermediates) released upon CO_3^{2-} decomposition. The involvement of carbonate intermediates is directly confirmed by the established correlation between the selectivity and the relative content of C^{18}O_2 and C^{16}O_2 in the CO-PROX reaction products. The nascent Mars van Krevelen mechanism of direct CO oxidation into CO_2 is coupled with the subsequent Langmuir-Hinshelwood/Eley-Rideal step, which is prompted by dissociative refilling of the oxygen vacancies by O_2 , leading to the formation of O_{ads} . In addition to the carbonate/bicarbonate pathways, hydrogen may also be oxidized in parallel by interaction with O_{ads} or O_{surf}^{2-} . This route is responsible for the loss of selectivity of B-type spinels in the low temperature range, whereas electroprotic oxidation of H_2 by O_{surf}^{2-} leads to a decrease in the selectivity of the A-type spinels in the high temperature range. The applied heuristic approach allows for elucidation of the CO-PROX reaction progress in terms of the three concurrent generic mechanistic cycles.

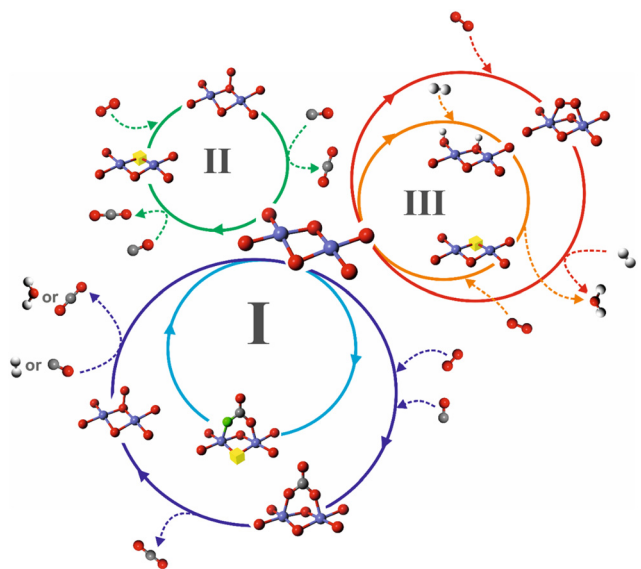


Fig. 11 Functional model illustrating the three main catalytic cycles involved in the CO-PROX reaction. I – carbonate cycle, II – direct oxidation of CO by lattice oxygen, and III – direct oxidation of H_2 *via* the LH/ER (red circle) or EP (orange circle) mechanism.



Author contributions

The manuscript was written through contributions of all the authors. All the authors have given approval to the final version of the manuscript.

Conflicts of interest

The authors declare no competing interests.

Acknowledgements

This work was supported by the Polish National Science Center (NCN) Project OPUS-14, No 2017/27/B/ST4/01155. Camillo Hudy was partially supported by the doctoral EU Project POWR.03.02.00-00-I004/16. The open-access publication of this article was funded by the program "Excellence Initiative – Research University" at the Jagiellonian University in Krakow.

References

- 1 T. V. Choudhary and D. W. Goodman, *Catal. Today*, 2002, **77**, 65–78.
- 2 E. D. Park, D. Lee and H. C. Lee, *Catal. Today*, 2009, **139**, 280–290.
- 3 H. Wang, H. Zhu, Z. Qin, G. Wang, F. Liang and J. Wang, *Catal. Commun.*, 2008, **9**, 1487–1492.
- 4 N. Bion, F. Epron, M. Moreno, F. Mariño and D. Duprez, *Top. Catal.*, 2008, **51**, 76–88.
- 5 P. Jing, X. Gong, B. Liu and J. Zhang, *Catal. Sci. Technol.*, 2020, **10**, 919–934.
- 6 A. Martínez-Arias, D. Gamarra, M. Fernández-García, A. Hornes, P. Bera, Z. Koppány and Z. Schay, *Catal. Today*, 2009, **143**, 211–217.
- 7 A. Davó-Quiñonero, E. Bailón-García, S. López-Rodríguez, J. Juan-Juan, D. Lozano-Castelló, M. García-Melchor, F. C. Herrera, E. Pellegrin, C. Escudero and A. Bueno-López, *ACS Catal.*, 2020, **10**, 6532–6545.
- 8 S. Dey and G. C. Dhal, *Mater. Today Chem.*, 2019, **14**, 100180.
- 9 H. F. Wang, R. Kavanagh, Y. L. Guo, Y. Guo, G. Lu and P. Hu, *J. Catal.*, 2012, **296**, 110–119.
- 10 Z. Li, H. Wang, X. Wu, Q. Ye, X. Xu, B. Li and F. Wang, *Appl. Surf. Sci.*, 2017, **403**, 335–341.
- 11 S. Royer and D. Duprez, *ChemCatChem*, 2010, **3**, 24–65.
- 12 Z. Zhao, M. M. Yung and U. S. Ozkan, *Catal. Commun.*, 2008, **9**, 1465–1471.
- 13 F. Arena, F. Ferrante, R. Di Chio, G. Bonura, F. Frusteri, L. Frusteri, A. Prestianni, S. Morandi, G. Martra and D. Duca, *Appl. Catal., B*, 2022, **300**, 120715.
- 14 F. Mariño, C. Descorme and D. Duprez, *Appl. Catal., B*, 2005, **58**, 175–183.
- 15 L. Zhong, M. Barreau, V. Caps, V. Papaefthimiou, M. Hävecker, D. Teschner, W. Baaziz, E. Borfecchia, L. Braglia and S. Zafeiratos, *ACS Catal.*, 2021, **11**, 5369–5385.
- 16 G. Avgouropoulos, T. Ioannides, H. K. Matralis, J. Batista and S. Hocevar, *Catal. Lett.*, 2001, **73**, 33–40.
- 17 A. Martínez-Arias, M. Fernández-García, J. Soria and J. C. Conesa, *J. Catal.*, 1999, **182**, 367–377.
- 18 S. S. Maluf and E. M. Assaf, *Catal. Commun.*, 2011, **12**, 703–706.
- 19 B. Viswanathan, *Catal. Rev.: Sci. Eng.*, 1992, **34**, 337–354.
- 20 P. V. Gosavi and R. B. Biniwale, *Int. J. Hydrogen Energy*, 2012, **37**, 3958–3963.
- 21 C. A. Chagas, E. F. De Souza, M. C. N. A. De Carvalho, R. L. Martins and M. Schmal, *Appl. Catal., A*, 2016, **519**, 139–145.
- 22 T. Valdés-Solís, I. López and G. Marbán, *Int. J. Hydrogen Energy*, 2010, **35**, 1879–1887.
- 23 L. Lukashuk, K. Föttinger, E. Kolar, C. Rameshan, D. Teschner, M. Hävecker, A. Knop-Gericke, N. Yigit, H. Li, E. McDermott, M. Stöger-Pollach and G. Rupprechter, *J. Catal.*, 2016, **344**, 1–15.
- 24 M. Che and A. J. Tench, *Characterization and Reactivity of Molecular Oxygen Species on Oxide Surfaces*, 1983, vol. 32.
- 25 M. Anpo, G. Costentin, E. Giamello, H. Lauron-Pernot and Z. Sojka, *J. Catal.*, 2021, **393**, 259–280.
- 26 E. Giamello, Z. Sojka, M. Che and A. Zecchina, *J. Phys. Chem.*, 1986, **90**, 6084–6091.
- 27 C. Hudy, O. Długosz, J. Grybos, F. Zasada, A. Krasowska, J. Janas and Z. Sojka, *Catal. Sci. Technol.*, 2022, **12**, 2446–2461.
- 28 T. M. Nyathi, N. Fischer, A. P. E. York and M. Claeys, *ACS Catal.*, 2020, **10**, 11892–11911.
- 29 M. P. Yeste, H. Vidal, A. L. García-Cabeza, J. C. Hernández-Garrido, F. M. Guerra, G. A. Cifredo, J. M. González-Leal and J. M. Gatica, *Appl. Catal., A*, 2018, **552**, 58–69.
- 30 P. T. A. Santos, H. L. Lira, L. Gama, F. Argolo, H. M. C. Andrade and A. C. F. M. Costa, *Mater. Sci. Forum*, 2010, **660–661**, 771–776.
- 31 K. Omata, T. Takada, S. Kasahara and M. Yamada, *Appl. Catal., A*, 1996, **146**, 255–267.
- 32 Q. Guo and Y. Liu, *Appl. Catal., B*, 2008, **82**, 19–26.
- 33 M. Jin, Z. Li, W. Piao, J. Chen, L. Y. Jin and J. M. Kim, *Catal. Surv. Asia*, 2017, **21**, 45–52.
- 34 A. Elmhamdi, L. Pascual, K. Nahdi and A. Martínez-Arias, *Appl. Catal., B*, 2017, **217**, 1–11.
- 35 Z. Zhao, X. Lin, R. Jin, Y. Dai and G. Wang, *Catal. Commun.*, 2011, **12**, 1448–1451.
- 36 G. Grzybek, K. Ciura, J. Gryboś, P. Indyka, A. Davó-Quiñonero, D. Lozano-Castelló, A. Bueno-Lopez, A. Kotarba and Z. Sojka, *J. Phys. Chem. C*, 2019, **123**, 20221–20232.
- 37 H. Tanaka, M. Kuriyama, Y. Ishida, S. I. Ito, K. Tomishige and K. Kunimori, *Appl. Catal., A*, 2008, **343**, 117–124.
- 38 Y. Yu, T. Takei, H. Ohashi, H. He, X. Zhang and M. Haruta, *J. Catal.*, 2009, **267**, 121–128.
- 39 F. Zasada, J. Janas, W. Piskorz, M. Gorczyńska and Z. Sojka, *ACS Catal.*, 2017, **7**, 2853–2867.
- 40 F. Zasada, J. Gryboś, E. Budiyanto, J. Janas and Z. Sojka, *J. Catal.*, 2019, **371**, 224–235.
- 41 L. Zhong, T. Kropp, W. Baaziz, O. Ersen, D. Teschner, R. Schlögl, M. Mavrikakis and S. Zafeiratos, *ACS Catal.*, 2019, **9**, 8325–8336.
- 42 J. Jansson, A. E. C. C. Palmqvist, E. Fridell, M. Skoglundh, L. Osterlund, P. Thormahlen and V. Langer, *J. Catal.*, 2002, **211**, 387–397.



- 43 A. Beniya, K. Miwa, H. Hirata, Y. Watanabe and S. Higashi, *ACS Catal.*, 2022, **12**, 1977–1985.
- 44 T. M. Nyathi, N. Fischer, A. P. E. E. York, D. J. Morgan, G. J. Hutchings, E. K. Gibson, P. P. Wells, C. R. A. Catlow and M. Claeys, *ACS Catal.*, 2019, **9**, 7166–7178.
- 45 M. Khasu, T. Nyathi, D. J. Morgan, G. J. Hutchings, M. Claeys and N. Fischer, *Catal. Sci. Technol.*, 2017, **7**, 4806–4817.
- 46 S. Bac and S. Mallikarjun Sharada, *ACS Catal.*, 2022, **12**, 2064–2076.
- 47 S. Huang, K. Hara and A. Fukuoka, *Chem. – Eur. J.*, 2012, **18**, 4738–4747.
- 48 R. Zhang, T. Haddadin, D. P. Rubiano, H. Nair, C. S. Polster and C. D. Baertsch, *ACS Catal.*, 2011, **1**, 519–525.
- 49 M. Shou and K. I. Tanaka, *Catal. Lett.*, 2006, **111**, 115–118.
- 50 *EUROKIN Spreadsheet on Requirements for Measurement of Intrinsic Kinetics in the Gas-solid Fixed-bed Reactor*, <https://www.eurokin.org>.
- 51 P. V. B. Pinho, J. Grybos, C. Hudy, J. Janas, K. Góra-Marek, F. Zasada and Z. Sojka, *Appl. Surf. Sci.*, 2020, **513**, 145835.
- 52 F. Zasada, J. Janas, W. Piskorz and Z. Sojka, *Res. Chem. Intermed.*, 2017, **43**, 2865–2880.
- 53 J. P. Perdew, K. Burke and M. Ernzerhof, *Phys. Rev. Lett.*, 1996, **77**, 3865–3868.
- 54 H. J. Monkhorst and J. D. Pack, *Phys. Rev. B: Solid State*, 1976, **13**, 5188–5192.
- 55 F. Zasada, W. Piskorz, S. Cristol, J. F. Paul, A. Kotarba and Z. Sojka, *J. Phys. Chem. C*, 2010, **114**, 22245–22253.
- 56 T. Hirano, *MOPAC Manual*, 7th edn, 1993.
- 57 L. Lukashuk, N. Yigit, R. Rameshan, E. Kolar, D. Teschner, M. Hävecker, A. Knop-Gericke, R. Schlögl, K. Föttinger and G. Rupprechter, *ACS Catal.*, 2018, **8**, 8630–8641.
- 58 H. F. Wang, R. Kavanagh, Y. L. Guo, Y. Guo, G. Z. Lu and P. Hu, *Angew. Chem., Int. Ed.*, 2012, **51**, 6657–6661.
- 59 A. Cárdenas-Arenas, A. Quindimil, A. Davó-Quiñonero, E. Bailón-García, D. Lozano-Castelló, U. De-La-Torre, B. Pereda-Ayo, J. A. González-Marcos, J. R. González-Velasco and A. Bueno-López, *Appl. Catal., B*, 2020, **265**, 118538.
- 60 J. Mascetti and M. Tranquille, *J. Phys. Chem.*, 1988, **92**, 2177–2184.
- 61 N. Macleod, R. Copley, J. M. Keel and R. M. Lambert, *J. Catal.*, 2004, **221**, 20–31.
- 62 K. Góra-Marek and J. Datka, *Catal. Today*, 2008, **137**, 466–470.
- 63 A. Davó-Quiñonero, M. Navlani-García, D. Lozano-Castelló, A. Bueno-López and J. A. Anderson, *ACS Catal.*, 2016, **6**, 1723–1731.
- 64 J. Y. Kim, J. A. Rodriguez, J. C. Hanson, A. I. Frenkel and P. L. Lee, *J. Am. Chem. Soc.*, 2003, **125**, 10684–10692.
- 65 C. M. Damaskinos, J. Zavašnik, P. Djinović and A. M. Efstathiou, *Appl. Catal., B*, 2021, **296**, 120321.
- 66 A. G. S. Hussien, C. M. Damaskinos, A. Dabbawala, D. H. Anjun, M. A. Vasiliades, M. T. A. Khaleel, N. Wehbe, A. M. Efstathiou and K. Polychronopoulou, *Appl. Catal., B*, 2022, **304**, 121015.

